Evaluation of Different Graphene Manufacturing: Structure, Composition, and Electrochemical Properties

by

Huiyi Yang

A thesis

presented to the University of Waterloo

in fulfillment of the

thesis requirement for the degree of

Master of Applied Science

in

Chemical Engineering – Nanotechnology

Waterloo, Ontario, Canada, 2023

© Huiyi Yang 2023

Author's Declaration

I hereby declare that I am the sole author of this thesis. This is a true copy of the thesis including any required final revisions, as accepted by my examiners.

I understand that my thesis may be made electronically available to the public.

Abstract

Graphene is a two-dimensional material composed of carbon atoms arranged in a hexagonal pattern. Its thickness is one atom, making it the thinnest material in existence. Graphene has unique properties that make it suitable for various applications. To commercialize graphene products, the industrial production process must meet specific requirements and provide advantages over other alternatives. The mass production method employed should be capable of delivering the required quantities while ensuring reliable quality for large-scale industrial applications. Several synthesis methods are currently utilized to produce graphene, including epitaxial growth, liquid phase exfoliation, electrochemical exfoliation, mechanical exfoliation, and chemical vapor deposition (CVD). Different techniques for synthesizing graphene have their benefits and drawbacks, which can vary depending on the intended use of the material. This study focused on evaluating three commonly used methods for synthesizing graphene: CVD, Hummer's graphene, and Organic Salt graphene. To determine the most appropriate application for each method, characteristic properties were compared using various characterization techniques such as XRD, Raman, BET, and FTIR. In addition, the conducted conductivity and electrochemical tests were performed to accurately assess their suitability for electronic and energy storage applications.

Keywords

Graphene synthesis, property characterization, application evaluation

Acknowledgments

I want to express my thankfulness to Dr. Aiping Yu, my supervisor, for giving me the precious opportunity to explore the world of nanomaterials, and for their continuous support and patient guidance throughout my master's study.

I am also grateful to my committee members, Dr. David Simakov and Dr. Yverick Pascal Rangom for providing valuable comments and suggestions on my project.

Furthermore, I would like to extend my heartfelt gratitude to my colleagues, especially Maiwen and Saeed, for their kindness and support that contributed significantly to my personal and professional growth. This project would not have been possible without the invaluable help and advice from Lan, Zhen, Rui, Tingzhou, Moon, Tyler, and Moin. Additionally, I am thankful for the daily companionship of Jing, Yu, Gaopeng, Myeong, Abel, Jingjing, and Qianyi, as well as the many others who have supported me around the University of Waterloo campus.

My feline companion, Landy has been a constant source of comfort and support, keeping me company during long hours of work over the past days and nights.

Lastly, I am deeply grateful to my mother and Jiahao for their constant and unwavering support and encouragement. Their unconditional belief in me has given me the courage and motivation to pursue my goals and strive towards achieving my dream life.

Dedication

For my family

Table of Contents

Author's Declaration ii

Abstract iii

Keywords iii

Acknowledgments iv

Dedication v

List of Figures viii

List of Tables x

Nomenclature xi

1.0 Introduction 1

2.0 Graphene 6

2.1 Synthesis Method 7

2.1.1 Mechanical Exfoliation method 10

2.1.2 Electrochemical Exfoliation 12

2.1.3 Chemical Reduction Method 13

2.1.4 Chemical Vapour Deposition 16

2.1.5 Pyrolysis of Organic Salts Method 18

2.1.6 Opening/Unzipping Carbon Nanotubes: Graphene Nanoribbons 20

3.0 Methodology 22

3.1 X-Ray Diffraction 22

3.2 Raman Spectroscopy 24

3.3 Fourier Transform Infrared Spectroscopy (FTIR) 27

3.4 Scanning Electron Microscope (SEM) 29

3.5 Brunauer-Emmett- Teller (BET) 31

3.6 Ultraviolet-Visible Spectroscopy (UV-vis) 33

4.0 Evaluation of Different Graphene Manufacturing: Structure, Composition, and Electrochemical Properties 35

4.1 Introduction and Project purpose 35

4.2 Experimental Section 36

4.2.1 Materials 36

4.2.2 Hummer's Graphene (HRGO) Synthesis 36

4.2.3 Organic Salts Graphene (OSG) Synthesis 37

4.2.4 Material Characterization 38

4.2.5 Conductivity Test 38

4.2.6 Electrochemical Characterization 39

4.3 Results and Discussion 41

5.0 Summary 57

6.0 Outlook 59

Reference 61

List of Figures

Figure 1: (a) Graphene chemical structure and physical properties [13] including all dimensionalities [14], (b) The milestone of the graphene commercialization. 5

Figure 2: (a) Graphene synthesis processes flow graph (b) Top down method and (c) Bottom up method (d) Unzipping carbon nanotube method [19]. 9

Figure 3: Benchtop XRD unit. 22

Figure 4: Bragg's law schematic. 23

Figure 5: Energy-level diagram showing the states involved in Raman spectra[60]. 25

Figure 6: Schematic of Raman spectrometer[62]. 26

Figure 7: Bench top Raman spectroscope unit. 26

Figure 8: Schematic sketch of the essential features of a Fourier transform infrared (FTIR) spectrometer [65]. 28

Figure 9: Nicolet 6700 spectrometer components [66]. 28

Figure 10: Schematic illustration of typical SEM setup [66]. 30

Figure 11: Schematic of BET surface analyzer [70]. 31

Figure 12: Types of adsorption isotherms [69]. 32

Figure 13: Basic block diagram of single beam UV-Vis spectrometer [71]. 34

Figure 14: Schematic of Improved Hummer's Method. 37

Figure 15: Schematic of Organic Salts method. 38

Figure 16: 4-point probe schematic view [74]. 39

Figure 17: Three-electrode system. 40

Figure 18: (a) XRD spectrum, (b) Raman Spectra, (c) FTIR spectra of CVDG, HRGO, OSG, GO and commercial graphite. 44

Figure 19: SEM images of OSG (a-c), HRGO (d-f) and CVD graphene (g-i). 45

Figure 20: Nitrogen adsorption/desorption isothermals for (a) GO, (b) OSG and (c) HRGO; Pore size distribution of (d) GO, (e) OSG and (f) HRGO. 47

Figure 21: Dispersion test of HRGO (left), and OSG (right) at 0, 1, 5, 24 hours. 48

Figure 22: UV-vis absorption spectra of HRGO and OSG nanosheets dispersed in water. 48

Figure 23: Represents (a-b) cyclic voltammetry curves, (c-d) galvanic charge-discharge curves of OSG (left), and HRGO (right). 51

Figure 24: Represents (a-b) electrochemical impedance spectroscopy plot, (c-d)) Cyclability curves of OSG (the left) and HRGO (the right). 54

Figure 25: An evaluation of various graphene and derivative products, considering the intrinsic properties based on yield, defect density, electrical conductivity, surface area, layer number, and cost. The ranking of low, medium, and high levels is represented by the number 1, 2, 3 respectively. 58

Figure 26: A diagram displaying various graphene synthesis method and some of their eventual applications. 60

List of Tables

Table 1: Parameters extracted from the XRD spectrum of CVDG, HRGO, OSG, GO and commercial graphite..... 41

Table 2: Parameters extracted from the Raman spectrum of CVDG, HRGO, OSG, GO and commercial graphite..... 43

Table 3: Summary of Direct current conductivity results..... 49

Table 4: Summary of cyclic voltammetry (CV) results..... 51

Table 5: Summary of galvanic charge-discharge (GCD)results..... 52

Table 6: A summary of the significant properties of for various applications. 56

Nomenclature

Latin Letters

B2B	Batch to Batch
BET	Brunauer-Emmett-Teller surface area analyzer
BSEs	Backscattered electrons
CVD	Chemical Vapor Deposition
CN/CA	Cellulose nitrate (CN) and cellulose acetate (CA)
CNT	Carbon Nanotubes
CV	Cyclic voltammetry
C_s	Specific Capacitance from CV curve
C_T	Specific Capacitance from GCD curve
DMF	Dimethylformamide
DC	Direct Current
d	Distance between adjacent atomic planes in the crystal lattice
EIS	Electrochemical Impedance Spectroscopy
FTIR	Fourier Transform Infrared Spectroscopy
GQDs	Graphene Quantum Dots
GCD	Galvanostatic Charge and Discharge
HRGO	Hummer's reduced Graphite Oxide
HOPG	Highly-Oriented Pyrolytic Graphite
I	Applied current
JCPDS	Joint Committee on Powder Diffraction Standards
L_x	Number of graphitic layers
L_a	Crystalline size
MWCNT	Multiwalled Carbon Nanotubes
n	Order of diffraction
OSG	Organic Salts Graphene
PFLG	Planar Few-Layer Graphene
PECVD	Plasma Enhanced Chemical Vapor Deposition
PTFE	Poly tetrafluoroethylene

PVC	Polyvinyl chloride
PC	Polycarbonate
PET	Polyethylene terephthalate
PVDF	Polyvinyldifluoride
R2R	Roll to Roll
rGO	reduced Graphite Oxide
R	Electrical resistance
SEM	Scanning Electron Microscopy
SEs	Secondary electrons
t	Sample thickness
UV-vis	Ultraviolet-Visible Spectroscopy
XRD	X-Ray Diffraction

Greek Symbols

λ	Wavelength of the incident X-rays/ laser line wavelength used in the Raman experiment
ϑ	Angle between the incident X-ray beam and the plane of the crystal lattice
τ	The mean size of the crystalline domains
β	The full-width half-max (FWHM) of the crystalline peaks
σ	Electrical conductivity
ρ	Electrical resistivity

1.0 Introduction

Graphene has been experimentally studied for over 40 years [1]. The study of two-dimensional (2D) materials and graphene has a long history dating back to P. R. Wallace's 1947 paper on the physical bandgap of graphite, and Blakely's work in the 1960s and 1970s. However, the discovery of graphene in 2004 and the subsequent Nobel Prize in Physics awarded in 2010 created high expectations for the graphene as a material [2]. As one of the lightest and strongest materials, graphene has great potential to replace many existing commercial materials and revolutionize entire industries in the fields of energy storage materials, nanoelectronics, polymer engineering and sensing. As compared to graphite, the single-layer structure of graphene gives it several advantages, such as great Young's modulus (1.0 TPa) [3], high optical transmittance (97.7%) [4], high intrinsic charge mobility (250000 $cm^2/V/s$) [5], and competitive conductivity (more than 1000 S/cm) [4] (Fig. 1). In contrast, graphite, being a layered material, has lower conductivity (30 S/cm) due to inter-layer resistance between the graphene sheets, and it is relatively weak in the out-of-plane direction [6]. Although, graphite is still used in various applications like pencils and lubricants, while graphene's unique properties make it useful in a wide range of fields such as electronics, energy storage, catalysis, and filtration.

Nowadays, the graphene group has been largely developed. As the fundamental building material for graphitic allotropes, it can be wrapped up 0D fullerenes, rolled up into a carbon nanotube (1D) and stacked up into many layers graphite (3D) [6]. The choice of application is contingent upon the inherent properties of graphene. For example, 2D films and heterostructure possessed high crystal quality and homogeneous thickness that makes them a promising material for use in

electronics and spintronics, while powders usually had large surface areas with high porosity, and were suitable for improving the performance of battery, sensors and catalysts [7]. The synthesis of graphene refers to the process of creating or obtaining graphene with the desired size and quality. There are various methods for synthesizing graphene and its derivatives that have been established so far, including mechanical exfoliation, chemical synthesis, chemical exfoliation, epitaxial growth, and thermal chemical vapor deposition (CVD). These methods have been widely researched and studied.

Typically, the methods for producing large quantities of graphene can be grouped into two categories: (1) a top-down approach, and (2) a bottom-up approach. Some of the major top-down techniques include liquid-phase exfoliation, plasma etching, electrochemical exfoliation, laser ablation, ball milling, and chemical reduction. Liquid-phase exfoliation involves the use of solvents to disperse and separate graphene layers. Plasma etching uses high-energy plasma to etch graphene layers from a substrate. Electrochemical exfoliation utilizes an electric current to separate graphene layers from bulk material. Laser ablation involves the use of high-power lasers to vaporize a material and collect the resulting graphene sheets. Ball milling involves the grinding of a material with balls to produce smaller graphene particles. Chemical reduction utilizes chemical reactions to break down a bulk material into graphene. Conversely, in the bottom-up synthesis route, graphene is produced through the controlled growth of individual graphene sheets from carbon-containing precursors. This can be achieved through various methods such as CVD, thermal pyrolysis, and epitaxial growth. CVD involves the deposition of carbon-containing gases onto a substrate, where they react and form graphene layers. Thermal pyrolysis involves the decomposition of a carbon-containing precursor in the presence of heat. Epitaxial growth involves

the deposition of graphene onto a substrate with a similar crystal structure to encourage the growth of graphene layers. Frequently adopted production methods using both top-down and bottom-up strategies will be reviewed briefly in the sub-sections below.

At present, there are three main methods for synthesizing graphene. CVD and Hummer's method are widely used in large-scale industrial production of graphene [8], while the Organic Salts method, which has been proposed in recent years, is considered a potential and uncomplicated alternative. CVD method is a rapid and controllable bottom-up approach to create single- and few-layer graphene film on a metal surface (Ni, Cu, F). It usually uses methane as carbon source with a continuous supply of hydrogen gas. Afterwards, the as-prepared graphene can be transferred to different substrates by the wet-etching method. CVD produces high-quality graphene with fine control of film thickness, while it still suffers from high energy consumption, low yield and high cost of production [7][9]. In the industry, the large-scale manufacturing CVD process can be divided into two categories based on the synthesized products: inch-sized graphene wafers by batch-to-batch (B2B) [10] process and continuous graphene film by roll-to-roll (R2R) [11] process. In addition, comprehensive research has been made on the preparation of reduced graphene oxide from intercalation and oxidization of graphite (top-down approach), such as the widely used improved Hummer's Method. It mixed strong acids (sulfur and phosphoric acid) and potassium permanganate to increase the interlayer distance of graphite and modify the functional groups on the surface. The as-prepared graphene oxide (GO) completed the exfoliation and reduction after thermal shock and finally produced reduced graphene oxide (rGO) flakes/powder. Owing to the good yield and less time compared to previous methods, Hummer's method has become one of the most popular commercial methods of producing graphene powder (HRGO). However, producing

high defect rGO with high consumption of oxidizing chemicals would unavoidably deduct its feasibility and scalability in real-world applications [12]. Recently, a novel bottom-up method has been reported. It utilized solid salts as precursors, sodium citrate and sodium carbonate, to generate high-quality few-layer graphene powder after the cyclodehydration reaction [13]. Upon heating, the carboxyl group on citrate salts is easily broken from the nearby carbon backbone. Due to the presence of one hydroxyl group in sodium carboxylate monomers, the remaining parts eliminate water and are bound to form cyclized carbon atoms. With the help of Na_2CO_3, the connection between the carbon p-electron species would be strengthened towards in-plane rearrangement, decreasing graphene layer number and producing high-quality graphene (OSG).

In this thesis, the correlation between a material's properties and its synthesis methods will be explored. Specifically, commonly used techniques for synthesizing graphene will be reviewed to provide readers with a comprehensive understanding of the pros and cons of each method. Additionally, three representative methods were tested in the laboratory, and the physical, chemical, and electrochemical properties of the resulting graphene types will be analyzed. A detailed assessment and comparison of their potential applications in various industrial fields, taking into account their unique characteristics and demands, will also be presented.

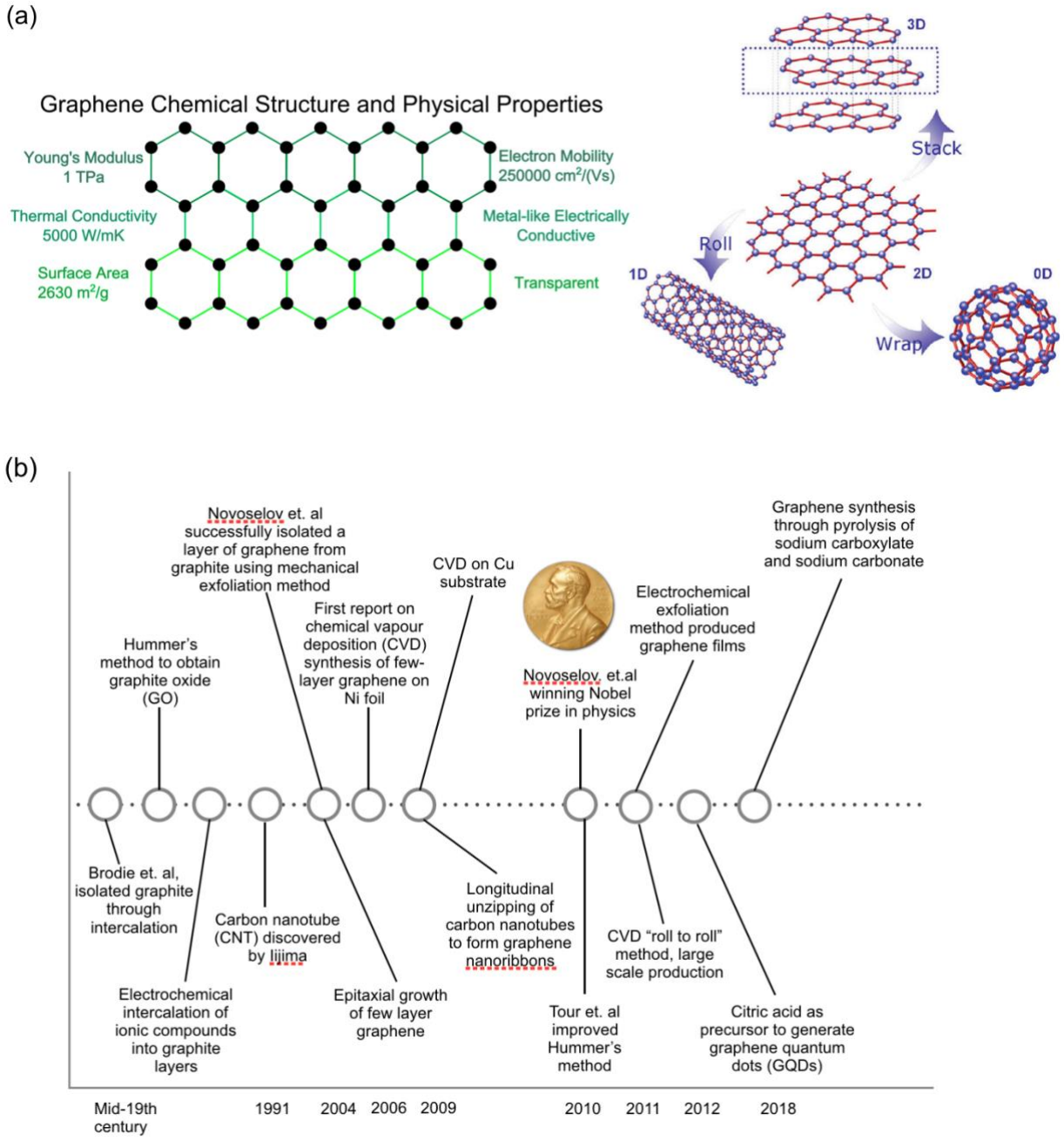


Figure 1: (a) Graphene chemical structure and physical properties [13] including all dimensionalities [14], (b) The milestone of the graphene commercialization.

2.0 Graphene

While graphite has been known for centuries, graphene was only discovered relatively recently, in 2004, using a mechanical exfoliation technique by scientists at the University of Manchester. As a single/few layers of the graphite structure, graphene and graphite are both made up of carbon atoms and share some similar properties. However, their distinct structures and properties make them more suitable for different applications. For example, graphene is an excellent conductor of electricity and heat, is incredibly strong and lightweight, and has a large surface area, making it ideal for use in electronics, energy storage, and water filtration. Graphite, on the other hand, has a layered structure that makes it soft, slippery, and brittle. Graphite is often used as a lubricant, in pencils, and in other industrial applications where its properties are useful.

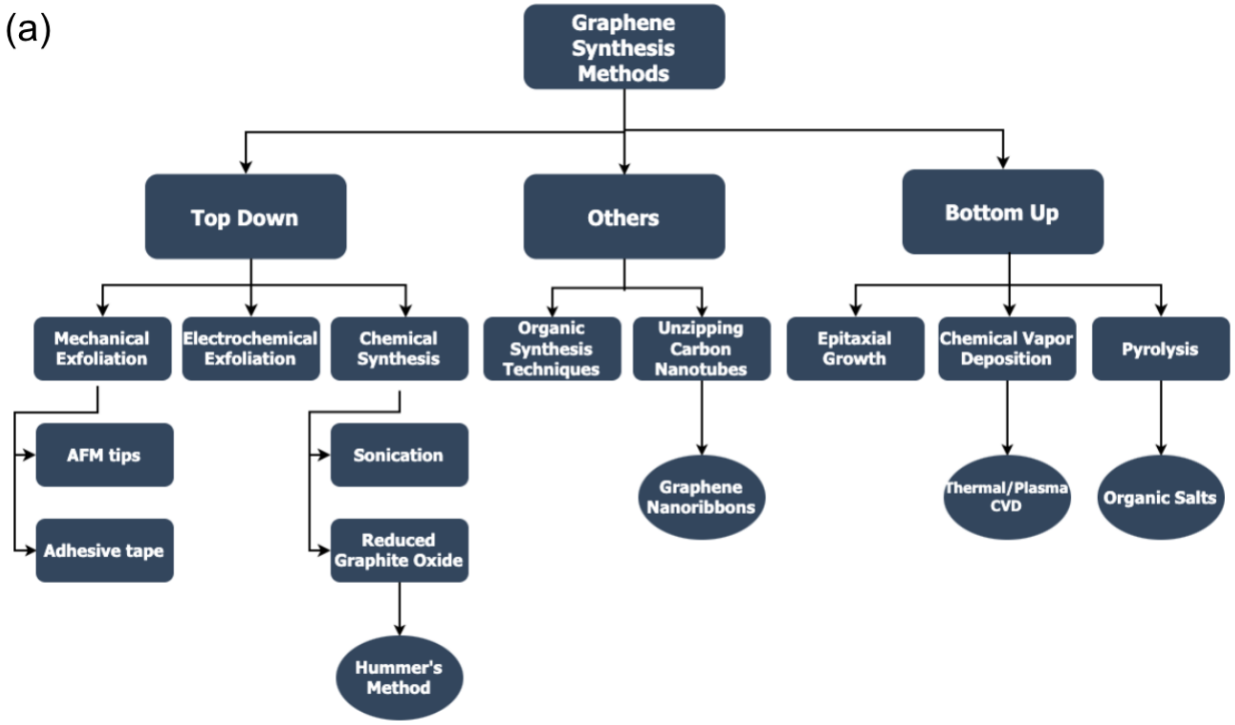
Over the last 15 years, most of the research and experimentation focused on graphene has been conducted in university laboratories and government-funded initiatives, with the ultimate objective of creating practical applications for commercial use. The customers who were quick to embrace this technology are leaders in the market for coatings that are resistant to corrosion and wear [2]. Recently, Ford Motor Company is using regenerated graphene to enhance the polyurethane foam in their new vehicles, resulting in increased tensile strength and noise absorption by at least a quarter. This is achieved using only 0.1% or less of graphene [14].

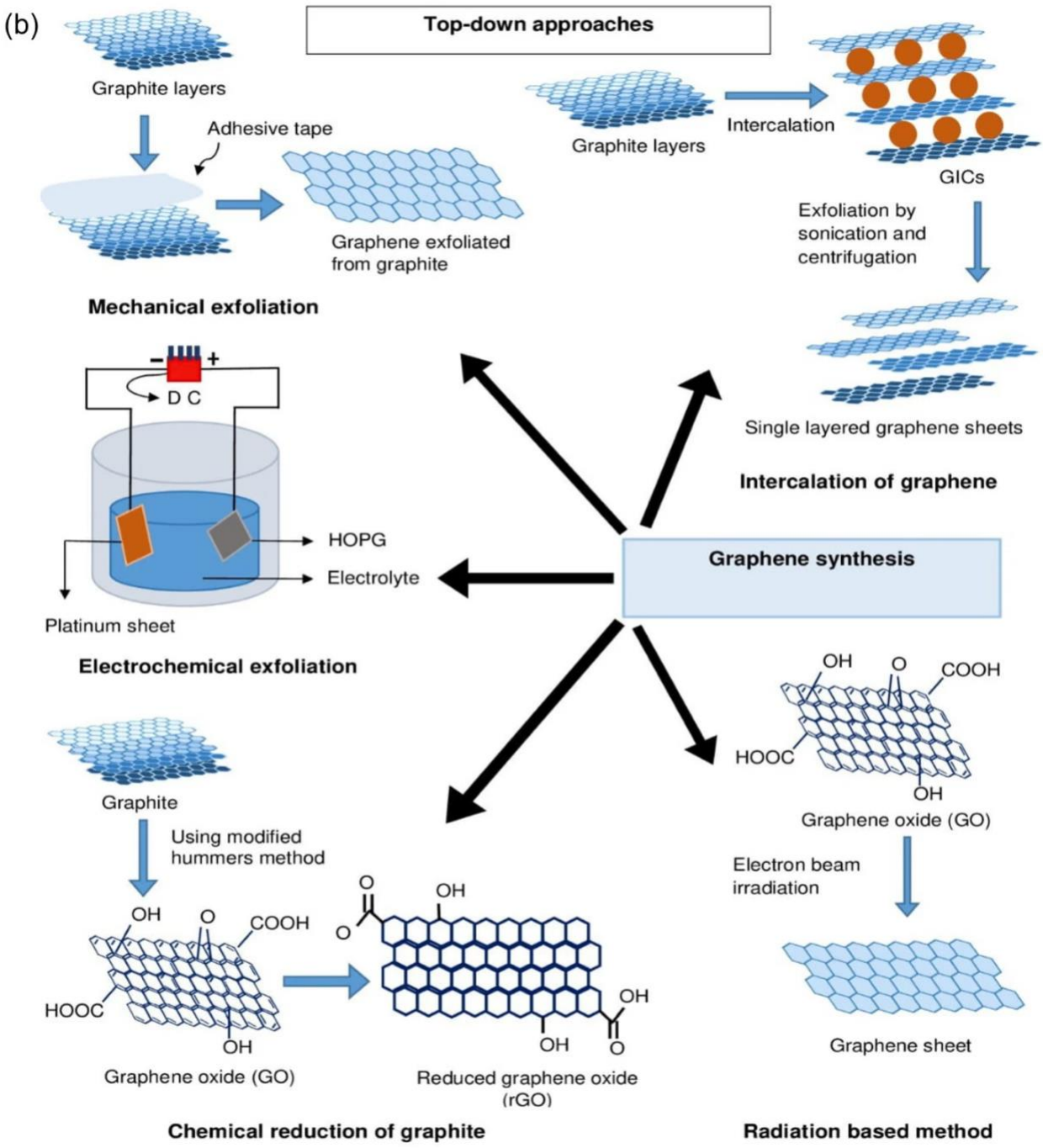
Graphene properties can be affected by several factors including the number of layers, defects and impurities [15], domain size and shape [16], doping [9], substrate [17], and strain. The need for high-quality graphene in bulk quantities for both industry and academia is crucial to meet demand and propel the material into commercial applications. In response, numerous preparation strategies

have been proposed in the literature, and many of these are already being used by companies that supply graphene.

2.1 Synthesis Method

The synthesis of graphene usually follows two approaches: "Top-down" and "Bottom-up." The former involves breaking down precursor graphene (graphite) into atomic layers, while the latter uses carbon molecules as building blocks, usually from conventional or alternative sources. While the bottom-up approach may not be suitable for producing large surface area graphene sheets, it can be used to produce significant quantities of graphene nanoribbons and nanoflakes. The methods for synthesizing graphene can be divided into various parts, as shown in Fig. 2.




(b)
Top-down approaches
Graphite layers
Adhesive tape
Graphene exfoliated from graphite
Mechanical exfoliation
Graphite layers
Intercalation
GICs
Exfoliation by sonication and centrifugation
Single layered graphene sheets
Intercalation of graphene
D C
HOPG
Electrolyte
Platinum sheet
Electrochemical exfoliation
Graphene synthesis
Graphite
Using modified hummers method
OH
O
COOH
HOOC
OH
Graphene oxide (GO)
Graphene oxide (GO)
Reduced graphene oxide (rGO)
Chemical reduction of graphite
Electron beam irradiation
Graphene sheet
Radiation based method

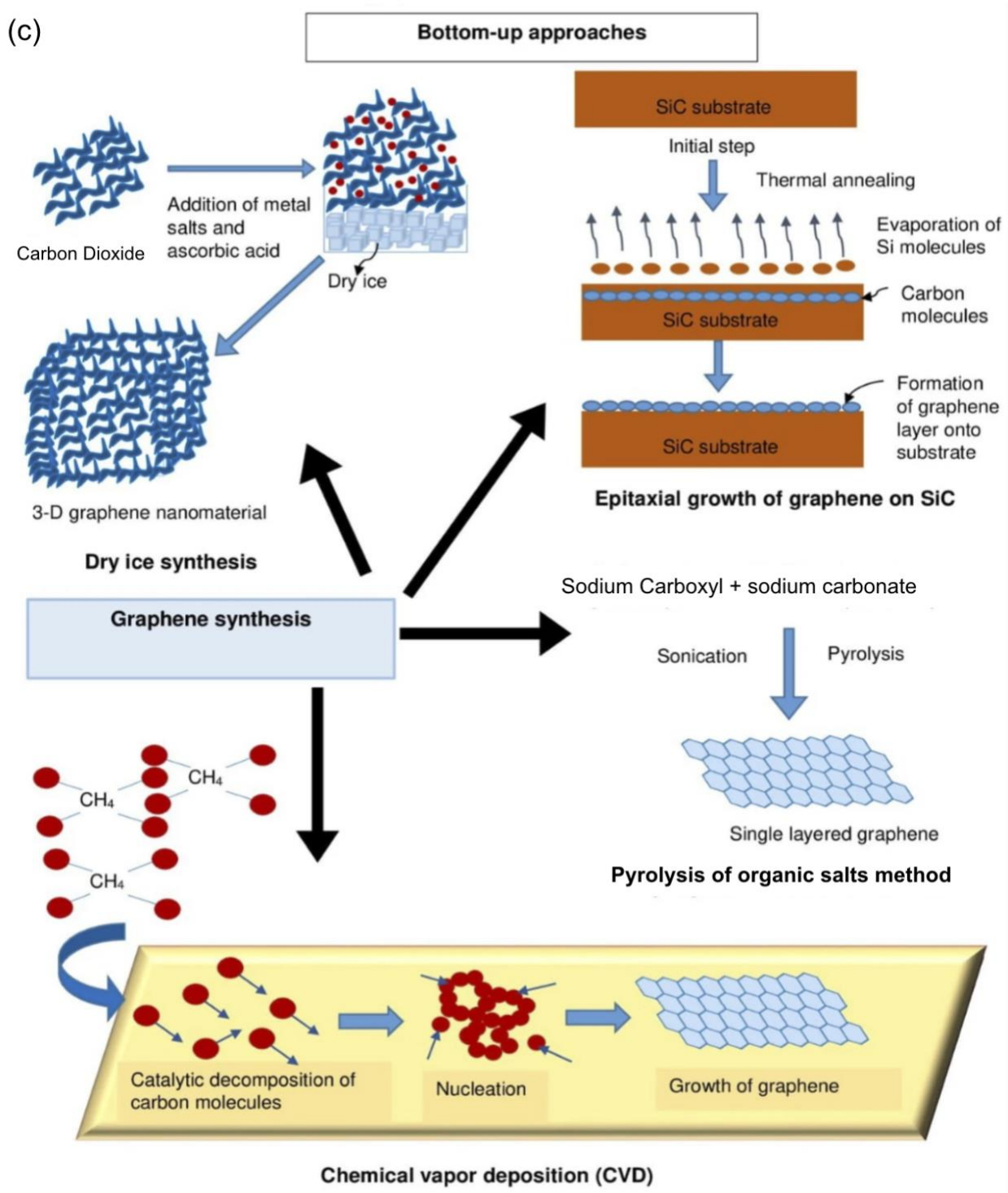


Figure 2: (a) Graphene synthesis processes flow graph (b) Top down method and (c) Bottom up method (d) Unzipping carbon nanotube method [19].

2.1.1 Mechanical Exfoliation method

Andrei Geim and Kostya Novoselov pioneered the use of a mechanical exfoliation method to successfully isolate a layer of graphene from highly-oriented pyrolytic graphite (HOPG) in 2004, thereby introducing the top-down concept [18]. Ideally, graphene should be separated from the bulk graphite layer in a layer-by-layer manner. Graphite is composed of monolayers of graphene that are held together by weak van der Waals forces. The interlayer distance between the graphene layers is 3.34 Å, and the bonding energy is 2 eV/nm^2 [19]. These weak interactions are due to the partially filled π orbitals that are perpendicular to the plane of the graphene sheets. As a result, the stacking of these sheets into graphite is also weak, involving van der Waals forces. This weak stacking allows for the easy separation of graphene sheets from the bulk graphite, resulting in the production of high-quality graphene flakes. To remove a monolayer graphene from graphite using mechanical cleaving, an external force of approximately 300 $N\mu m^{-2}$ is required.

Generally, it can be achieved by two kinds of mechanical approaches to exfoliate graphite into graphene flakes, namely normal force and lateral force [20]. One can apply normal force to overcome the van der Waals attraction between two graphite layers. This can be done through a technique known as micromechanical cleavage, in which a sharp tool or adhesive tape is used to peel off thin layers of graphene from the bulk graphite [21]. In 2015, Hang and his colleagues described a modified method for producing graphene. They used Scotch Tape to extract graphene flakes from a HOPG crystal. They then transferred the graphene flakes onto a plasma-cleaned SiO_2/Si substrate with an oxide thickness of 300 nm, and annealed them for 2-5 minutes at about 100°C on a hot plate. Finally, they peeled off the tape, resulting in the transfer of graphene flakes with a thickness of 1 to 4 layers onto the substrate [22]. Alternatively, one can employ lateral force

to facilitate the relative movement of two graphite layers by taking advantage of graphite's self-lubricating property in the lateral direction. This can be done through techniques such as ball milling, shear mixing, ultrasonication, and high-pressure homogenization, which use different forms of mechanical energy to separate the graphene layers [23]. In 2008, Hernandez and colleagues used organic solvents that has similar surface energy with graphene to synthesize large amounts of graphene films. They dispersed graphite powder in an organic solvent by bath sonication, followed by centrifugation to remove large aggregates. The remaining graphene layers were deposited on SiO_2 substrates by spray coating [24]. Later on, Bourlinos and his team utilized liquid-phase exfoliation via sonication in an ultrasound bath to exfoliate fine graphite powder in 2009 [25]. Ball milling is a frequently used method for exfoliation, where the shear force and collisions from rolling balls cause fragmentation of graphite flakes, potentially even destroying their crystalline structure. Wet ball milling requires solvents, while dry ball milling uses chemically inert, water-soluble inorganic salts [20]. In general, these methods rely on the shear forces generated by the mechanical energy to break the weak van der Waals bonds between the graphene layers and promote exfoliation.

Mechanical exfoliation is a simple, low-cost method for producing high-quality graphene flakes with well-defined edges and high electrical conductivity, suitable for electronic and optoelectronic applications. It is also beneficial for research and development purposes due to the ability to produce small quantities. However, it is time-consuming, requires skill, and produces a low yield of graphene flakes. The thickness and size of the flakes produced using this method are difficult to control, which limits their applications in certain fields.

2.1.2 Electrochemical Exfoliation

Electrochemical exfoliation relies on using electrodes made of graphitic carbon allotropes (such as graphite rods, carbon sheets, or highly oriented pyrolytic graphite) and electrolytes containing ionic liquid and poly(sodium-4-styrenesulfonate) aqueous solution. For example, In 2008, Liu et al. achieved complete exfoliation of graphite into individual graphene nanosheets using $[C_8mim]^+[PF_6]^-$ and water electrolyte, a 15 V potential, producing crumpled sheets measuring up to 700 nm in length, 500 nm in width, and 1.1 nm in average thickness [26].

The electrochemical exfoliation method comprises two main steps. Firstly, electrolyte intercalation and decomposition cause the bulk graphite to stretch macroscopically, generating gas and resulting in a highly expanded structure. Specifically, to promote structural expansion inside graphitic precursors, a liquid conductive electrolyte and a direct current are utilized. Under an electric field, a graphite electrode can undergo positive or negative intercalation, and can be further exfoliated by gases produced from solvent electrolysis or through post-treatment methods [27]. Secondly, exfoliated material is detached from the bulk solid and dispersed in solution as a consequence of the gas eruption. Graphite-intercalation compounds can be formed through anodic oxidation of water, hydroxylation or oxidation of graphite edge planes, intercalation of ionic liquid anions between graphite layers, and oxidative cleavage and precipitation of the compounds [26].

Overall, this method is scalable, meaning it can be easily scaled up or down depending on the desired quantity of graphene needed. It is also controllable, allowing for precise control over the thickness and quality of the graphene produced. Moreover, electrochemical exfoliation results in graphene having well-defined edges, and making it suitable for various applications such as energy

storage and conversion, and sensors. Additionally, the method can be performed under ambient conditions, making it environmentally friendly [26].

However, the process of electrochemical exfoliation is complex and requires specialized equipment and expertise. Fabricating graphene with a uniform size and layer distribution remains a challenge. The use of anodic potentials to intercalate ions can lead to undesired graphite oxidation and the introduction of oxygen functional groups, which disrupt the sp2-hybridized carbon network. The yield of graphene is typically lower compared to other methods [28], which can be a drawback for large-scale production. This process is mostly irreversible, as neither electrochemical nor chemical processes can fully restore the sp2-hybridized carbon network to the state of pristine graphene. Additionally, the presence of both structural damage and oxygen functional groups can significantly impact the electrochemical properties of the resulting graphene [26]. As a result, researchers continue to explore and improve upon this method to optimize its efficiency and performance for graphene production.

2.1.3 Chemical Reduction Method

Graphene production is commonly achieved by reducing graphene oxide, which is derived from oxidized graphite. In 1859, Brodie utilized potassium chlorate as an oxidant in his quest to establish the precise formula of graphite by creating highly oxidized graphite. Oxidative intercalation using potent oxidizing agents in concentrated sulfuric and nitric acids is a well-known technique for expanding graphitic layers. The resulting oxidized graphite had several oxygen functional groups distributed throughout the graphitic structure, thus incorporating sp^3-hybridized carbon atoms into the sp^2 hybridized carbon network of graphite [29].

Subsequent to Brodie's initial work, the method for expanding graphitic layers through oxidative intercalation was refined and improved by several researchers in chronological order. Staudenmaier (1898), Hofmann and König (1937), Hummers and Offeman (1958), and recently Tour and his team (2010) advanced the technique to obtain graphite oxide (GO). Staudenmaier and Hofmann and König employed potassium chlorate as the oxidizing agent, whereas Hummers and Offeman and Tour and his team used potassium permanganate instead to prevent the formation of hazardous, explosive ClO_2 gas [30]. Therefore, among the various methods for producing graphene oxide, Hummer's method has emerged as a leading commercial option. This is largely attributed to its ability to achieve high yields of graphene in a relatively short duration compared to earlier techniques. As a result, Hummer's method has gained significant popularity and is widely utilized for commercial production of graphene powder [8].

The oxygen functional groups present in graphite oxide and graphene oxide can be leveraged for chemical functionalization, resulting in the creation of new supporting materials for composites or sensor interfaces. However, if graphite oxide (or graphene oxide) is intended as a precursor for graphene production, additional steps are required to eliminate most, if not all, of the oxygen functional groups and restore the planar sp^2-hybridized carbon structure. Various techniques have been employed to accomplish this, including thermal, electrochemical, and chemical methods, which are the three main approaches used to remove the oxygen functional groups and restore the sp^2-hybridized carbon structure in graphene.

The thermal reduction method involves heating GO at around 1000 °C, which generates gaseous species and increases internal pressure, leading to the exfoliation of GO and elimination of oxygen

functional groups [31]. However, this method can also result in extended structural damage and defects. The resulting graphene is useful for applications like composite materials, ink, paint reinforcement, and electrochemical devices. The electrochemical reduction method, on the other hand, can eliminate most, but not all, electrochemically reducible oxygen functionalities, and it can be controlled easily under ambient conditions without toxic chemicals. Recent research has focused on controlling the C/O ratio in GO films using cathodic potentials. Structural variables like parent graphite particle size and oxygen functionalities affect the electrochemical properties of the resulting graphene materials [32]. Chemical agents are widely used to eliminate oxygen functional groups from GO and obtain reduced graphene sheets. The first reducing agent used was hydrazine in 1937, and its usage was recently reproposed to obtain reduced graphene with a C/O ratio of over 10 [33]. Other reducing agents include sodium borohydrate, lithium aluminum hydride, hydroquinone, hydroxylamine, L-ascorbic acid, saccharides, tea extract, wild carrot root, and even bacteria [30]. More recently, camera flashes [34] and laser scribes from commercial optical drives [35]were used to reduce GO films. The dispersibility of the reduced graphene sheets is often retained whenever possible.

The chemical reduction method is a scalable and attractive way to make graphene materials with improved electrical properties, high defect density, and edge like planes for fast electron transfer. These materials can be utilized in various applications including electrochemical sensors, energy storage devices, transparent conductive films, and composites. The properties of the graphene materials produced through chemical reduction can be diverse, depending on the type of reducing agents, starting GO material, and synthetic conditions used. Therefore, it is possible to produce chemically reduced graphene materials with distinct electrochemical properties. Chemical

exfoliation is a promising technique for synthesizing GO and reduced graphene oxide (rGO) for various commercial applications due to its ability to produce graphene in a controlled and scalable manner. However, the use of hazardous agents such as strong acids and elevated production temperatures can make this process less economical and less environmentally friendly compared to other commonly used graphene production methods.

2.1.4 Chemical Vapour Deposition

Recently, the production of high-quality graphene, consisting of a single or few layers and covering a large area, has been achieved using CVD. This method is considered one of the most promising techniques for industrial-scale graphene fabrication [8]. In CVD, a carbon source is heated to a high temperature in the presence of a transition-metal catalyst, which causes the carbon atoms to deposit and arrange into sp^2-hybridized carbon structures. Graphene is grown on metal surfaces, such as ruthenium, platinum, iridium, nickel, or copper [30]. Currently, nickel and copper are popular choices due to their low cost and high availability. The carbon source can be either a gaseous species like methane, ethane, or propane, or a solid source can also be used [36]. In 2006, the first report on CVD synthesis of planar few-layer graphene (PFLG) was published. Camphor, an environmentally-friendly and low-cost precursor, was used to synthesize graphene onto Ni foils. The process involved evaporating camphor at 180°C and then pyrolyzing it at 700-850°C using a carrier gas (usually argon) in a CVD furnace. After cooling at room temperature, few-layer graphene sheets were detected on the Ni foils [37].

Several types of CVD processes can be utilized depending on factors such as the quality, type of precursor, desired thickness, and structure of the product. These processes include thermal,

plasma-enhanced (PECVD), reactive, hot wall, and cold wall CVD [38]. In the hot wall process, the reactor walls are kept at a constant temperature throughout the reactor, while in the cold wall process, the walls remain unheated. The most commonly used CVD methods for graphene production are thermal CVD and PECVD [39]. However, in many cases, high-temperature deposition is not desirable, and plasma-assisted reaction and deposition have been employed to reduce the temperature required for the process.

The CVD process has several design components that can be tuned to optimize the growth of high-quality graphene. When using Ni as a substrate, the resulting graphene is highly polycrystalline due to carbon's higher solubility in Ni, resulting in uncontrolled orientation during the cooling process. In contrast, Cu allows the formation of larger monocrystalline areas of mostly single-layer graphene as a lower amount of carbon is dissolved. The presence of surface oxygen on Cu can also accelerate graphene growth, resulting in larger crystalline sizes [40]. However, the growth of graphene islands from different nucleation sites during the cooling process can result in the formation of grain/domain boundaries, which are defects in CVD graphene that can affect its properties. The precise tuning of deposition temperature, pressure, cooling time, and substrate quality can improve the production technique to enable the growth of mostly single-layer and large crystalline-sized graphene [30].

The transfer process is crucial for CVD graphene as it cannot be used without being transferred to an arbitrary surface and removing the metal catalyst substrate. The transfer process is done using polymer-supported metal etching/transfer or mechanical exfoliation with special functionalized polymers. However, this process can cause significant degradation of the graphene quality due to

the formation of wrinkles or structural damage from tearing and ripping [41]. The most common transfer method involves etching the metal substrate while the graphene is supported by an inert polymer. Other transfer substrates such as PTFE, PVC, PC, CN/CA, PET, paper, and cotton cloth have been investigated and applied via a hot/cold lamination process [42]. However, the transfer process can generate mechanical stress that causes structural damages and alterations and contribute to contamination by metallic impurities, which can dramatically alter the electronic properties of CVD graphene [30].

Despite its inferior electronic and structural properties compared to mechanically exfoliated graphene, CVD graphene has shown remarkable performance in various applications, including electronic transistors, transparent conductive electrodes, electrochemical devices, and corrosion-inhibiting coatings. It is important to note that if CVD graphene is used as an electrode material without being transferred, the quality of the graphene film formed on the metal catalyst substrate should be carefully evaluated. Even small fractures or holes in the graphene film could expose the metal catalyst to external agents, potentially leading to inaccurate evaluations of the electrochemical properties of the CVD graphene layer. This is because the exposed metal catalyst is redox active and can interact with the environment [43].

2.1.5 Pyrolysis of Organic Salts Method

A novel method for synthesizing graphene has been suggested, which involves using organic salt sodium citrate as a carbon source along with sodium carbonate to complete carbonization [13]. This technique draws inspiration from the bottom-up synthesis approach of GQDs, and some

unique organic precursors have demonstrated great potential for Graphene Quantum Dots (GQD) preparation via thermal pyrolysis or carbonization [44].

Researchers such as Li, Liu, and Loh have explored different methods of GQD synthesis, including stepwise solution chemistry [45], pyrolysis and exfoliation [46], and ruthenium surface-assisted synthesis using C60 molecules as a precursor [47]. Other non-conjugate organic precursors have also been considered for bottom-up GQD synthesis by carefully selecting diverse organic precursors and carbonization conditions. Tang et al. have reported a simple and effective microwave-assisted hydrothermal method for synthesizing size-tunable GQDs using glucose as the sole carbon source [48]. In a 2012 study, by adjusting the degree of carbonization of common organic precursor, citric acid, Dong et al. achieved blue luminescent GQDs resulting in nanosheets with specific dimensions and photoluminescent quantum yield of 9.0% [49].

Citric acid is frequently used as a source of carbon in bottom-up synthesis of carbon dots due to its ability to react with other organic compounds, likely because of the presence of three carboxyl groups and a hydroxyl group. It can be produced through bioprocesses using the fungus Aspergillus niger [50]. In the same way, the existence of a hydroxyl group in sodium carboxylate monomers causes the remaining parts to lose water and come together to create cyclized carbon atoms. Na_2CO_3 assists in strengthening the bond between the carbon P-electron species, resulting in an in-plane rearrangement that reduces the number of graphene layers and generates high-quality graphene. Hence, the main process that occurs in the production of single-layer graphene using the standard solid-state pyrolytic conversion technique involves the elimination of water through thermal cyclodehydration and the rearrangement of carbon atoms within the plane [13].

2.1.6 Opening/Unzipping Carbon Nanotubes: Graphene Nanoribbons

An alternative method from the top-down perspective involves opening or unzipping carbon nanotubes (CNTs) rather than using graphite as the initial material. Since a CNT is essentially a graphene layer rolled up, unzipping it can produce a long and narrow strip of graphene known as a "graphene nanoribbon" [17]. The capacity to modify the band gap by adjusting the width of graphene nanoribbons (GNRs) is a crucial characteristic. Thus, producing GNRs on a large scale with precise control over their width and length will promote their quick adoption and utilization in electronic devices. In this context, the longitudinal opening of CNTs is a compelling strategy since the nanotubes' circumference determines the nanoribbons' width [51].

Researchers have developed various methods to produceGNRs from multiwalled carbon nanotubes (MWCNTs). One method involves partially embedding MWCNTs on a layer of poly(methyl methacrylate) (PMMA) and treating them with an Ar plasma [52], while another method uses concentrated sulfuric acid and potassium permanganate to longitudinally unzip the nanotubes and introduce oxygen functionalities [53]. However, these methods may compromise the electronic properties of the GNRs due to structural damage. An alternative method involves a reductive process of heating MWCNTs in the presence of potassium, resulting in GNRs with a much lower defect density and comparable electronic properties to pristine graphene [54]. In addition, more methods have been proposed, including intercalation with Li-NH_3 followed by thermal exfoliation, catalytic unzipping with metal nanoparticles, and acidic oxidation treatment on flattened double-walled CNTs to control the unzipping process. The oxidative treatment on multiwalled CNTs can also lead to the unscrolling of the nanotubes to produce large graphene sheets [55]. A research study compared the electrochemical properties of GNRs obtained from

oxidative treatment and thermal exfoliation/reduction on stacked graphene nanofibers and multiwalled CNTs [56].

The studies mentioned above have shown that the electronic properties of graphene nanoribbons (GNRs) produced by unzipping carbon nanotubes (CNTs) are heavily affected by factors such as defect density, presence of oxygen groups, structural vacancies, and aspect ratios. Similarly, the electrochemical properties of GNRs produced using solution-based exfoliation, chemical oxidation/exfoliation, and reduction methods are also influenced by similar parameters. Additionally, the presence of metallic or carbonaceous impurities in the starting CNT material can significantly impact the electrochemical behavior of the resulting GNRs.

3.0 Methodology

3.1 X-Ray Diffraction

X-ray diffraction (XRD) is a non-destructive analytical technique used to determine the crystal structure and orientation of materials. The XRD equipment used in this project is shown in Fig. 3. A typical x-ray setup requires three basic elements: an x-ray tube, a sample holder and an x-ray detector. The experiment involves directing a beam of X-rays at the sample, which then scatters the X-rays in different directions. A detector is used to measure the intensity of the scattered X-rays at different angles. The resulting pattern of scattered X-rays is called a diffraction pattern. The diffraction pattern is used to determine the crystal structure of the material, including information about the unit cell size, lattice constants, and the arrangement of atoms within the crystal lattice. This information can be used to identify the material and determine its properties, such as its composition, phase, and crystallinity.



Figure 3: Benchtop XRD unit.

XRD test is based on the principle of Bragg's Law, firstly proposed by William Henry Bragg and William Lawrence Bragg in 1913 [57]. It states that when a beam of X-rays is incident on a crystalline material, the X-rays will be scattered at specific angles depending on the crystal lattice

structure of the material (as shown in Fig.4). The interlayer distance is an important parameter in determining the crystal structure and properties of a material. The distance between crystal planes can be calculated using Bragg's law (Eq.1) and the diffraction angle of the peak [57].

$$n\lambda = 2dsin\theta \qquad \textit{Equation 1}$$

where n is an integer representing the order of diffraction, λ is the wavelength of the incident X-rays, d is the distance between adjacent atomic planes in the crystal lattice, and θ is the angle between the incident X-ray beam and the plane of the crystal lattice.

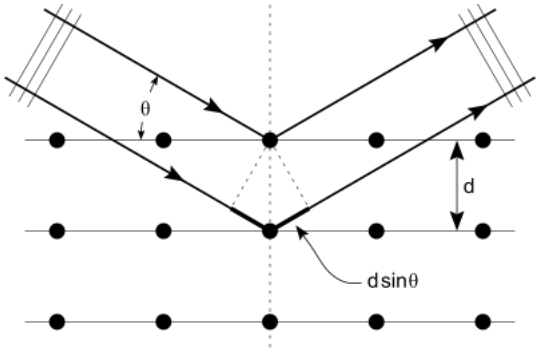


Figure 4: Bragg's law schematic.

Furthermore, the Scherrer equation can be used to estimate the size of the crystalline domains in a sample, including those on a nano-scale (Eq.2) [58]. To determine the FWHM and diffraction angle of characteristic peaks in nanoparticles, the diffraction peaks in the XRD spectra were analyzed using a Gaussian function curve-fitting method. The number of graphitic layers (L_x) present in the nanoparticles was calculated by dividing the crystal size by the interlayer distance (Eq. 3)

$$\tau = \frac{0.89\lambda}{\beta cos\theta} \qquad \textit{Equation 2}$$

$$L_x = \frac{\tau}{d} \qquad \textit{Equation 3}$$

Where τ is the mean size of the crystalline domains, λ is the incident x-ray wavelength, β is the full width half-max (FWHM) of the crystalline peaks and θ is the Bragg angle where the peak is found. In general, the larger the FWHM, the smaller the crystalline domains are.

Overall, XRD is typically regarded as a characterization method that does not cause damage to the sample being analyzed. It is also a fast technique that requires minimal preparation and can provide results that are clear and easy to interpret. However, XRD does have some limitations. It requires a reference to identify a sample and a minimum amount of material. It cannot determine the composition of an unknown sample on its own and only determines the crystal structure. Standard JCPDS card of known diffractograms is available for comparison and identification of unknown materials [59].

3.2 Raman Spectroscopy

Raman spectroscopy is a technique used in analytical chemistry and materials science to identify and characterize materials based on their molecular vibrations. It is a non-destructive method that can provide information about the chemical structure, composition, and physical properties of a sample.

The basic principle of Raman spectroscopy is the interaction of light with the chemical bonds of a molecule, which results in a change of its vibrational energy [60]. When a molecule interacts with light, it can produce an inelastically scattered photon that has either a higher or lower frequency than the incident photon (in Fig. 5). This phenomenon is called Raman scattering, and the higher frequency photons are known as anti-Stokes shifted photons, while the lower frequency photons

are called Stokes shifted photons. Most photons produced by the incident light undergo elastic scattering, which is useless for sample identification, and are filtered out. However, the Raman scattered photons are collected based on their frequency shift, and their intensity is plotted to generate a unique Raman spectrum for each molecule, which is determined by the vibrational, rotational, and stretching of the bonds.

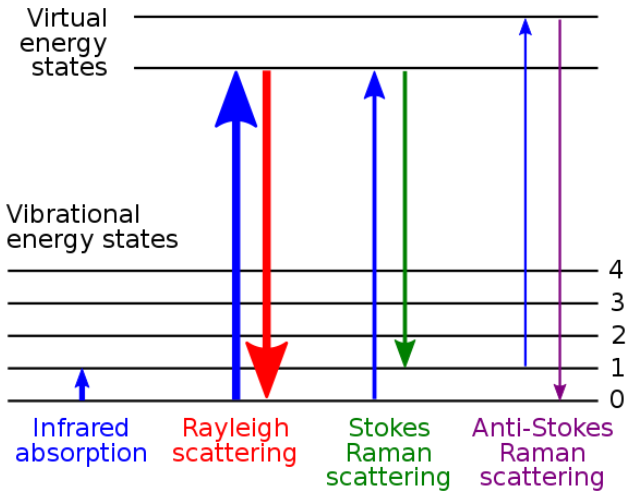


Figure 5: Energy-level diagram showing the states involved in Raman spectra[60].

In 1970, Knight and White compiled and analyzed the Raman spectra of different graphite systems [61]. Thus, they developed an empirical equation (Eq. 4) that enables the calculation of crystalline size, L_a, based on the ratio of the I_D and I_G peaks in the Raman spectra.

$$L_a(nm) = (2.4 \times 10^{-10})\lambda^4 \left(\frac{I_D}{I_G}\right)^{-1} \qquad \textit{Equation 4}$$

Where λ (in nm) is the laser line wavelength used in the Raman experiment.

A Raman spectrometer consists of a laser, a sample holder, and a detector, the schematic graph shown in Fig. 6. The laser is used to excite the sample, and the scattered light is collected and

analyzed to produce a Raman spectrum. The Raman spectrum is typically plotted as a graph of intensity versus wavelength or frequency, and contains peaks that correspond to the vibrational modes of the molecule. The equipment used in lab is shown in Fig. 7.

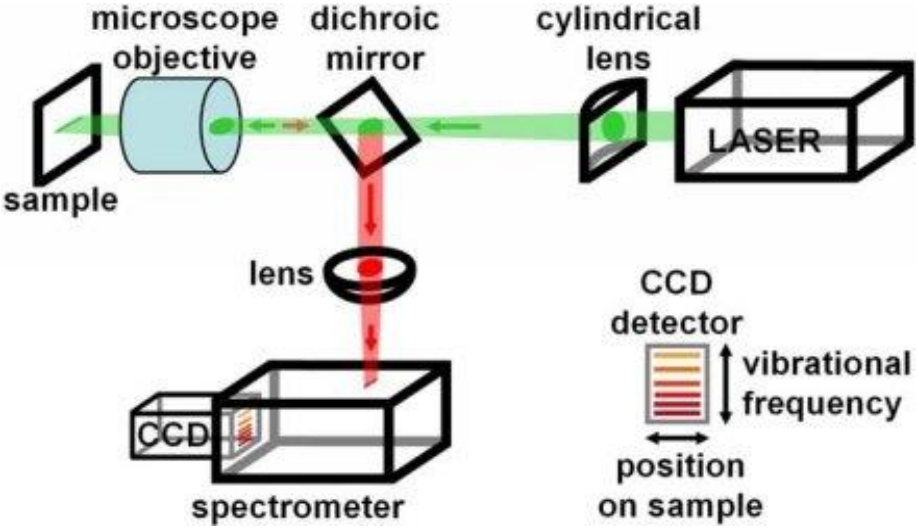


Figure 6: Schematic of Raman spectrometer [62].

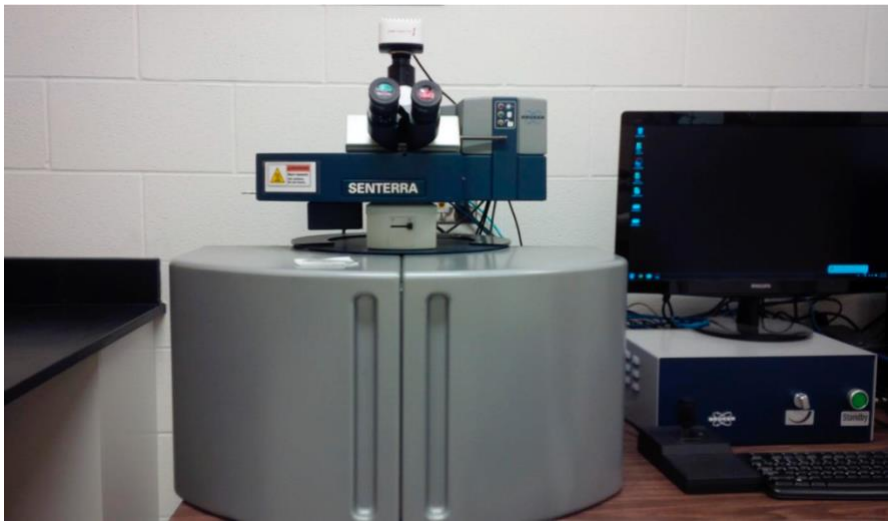


Figure 7: Bench top Raman spectroscope unit.

Generally, Raman spectroscopy is a fast and versatile technique, requiring minimal sample preparation. It can be used for in-situ analysis, making it a valuable tool for real-time monitoring

of chemical reactions and processes. However, it also has some limitations, including sensitivity to fluorescence, limited depth of penetration, and expense [62].

3.3 Fourier Transform Infrared Spectroscopy (FTIR)

FTIR is a powerful analytical technique used to study the vibrational modes of molecules in the infrared region of the electromagnetic spectrum [63]. When infrared radiation is absorbed by a sample, the energy of the radiation is transferred to the sample, causing the molecules in the sample to vibrate in a characteristic manner. The absorption of infrared radiation is determined by the chemical bond and the atomic weight of the atoms at either end of the bond.

FTIR instruments use an infrared light source, which is split by a beamsplitter into two beams, with one passing through the sample and the other not (Fig. 8). A detector measures the resulting interference pattern, and a computer performs a Fourier transform to obtain the infrared spectrum of the sample. FTIR instruments also include software for data analysis and calibration standards to ensure accuracy and reproducibility of the measurements [64]. The resulting spectrum is a plot of the intensity of the absorbed radiation as a function of the frequency or wavelength. Fig. 9 shows the detailed components of equipment applied in this study.

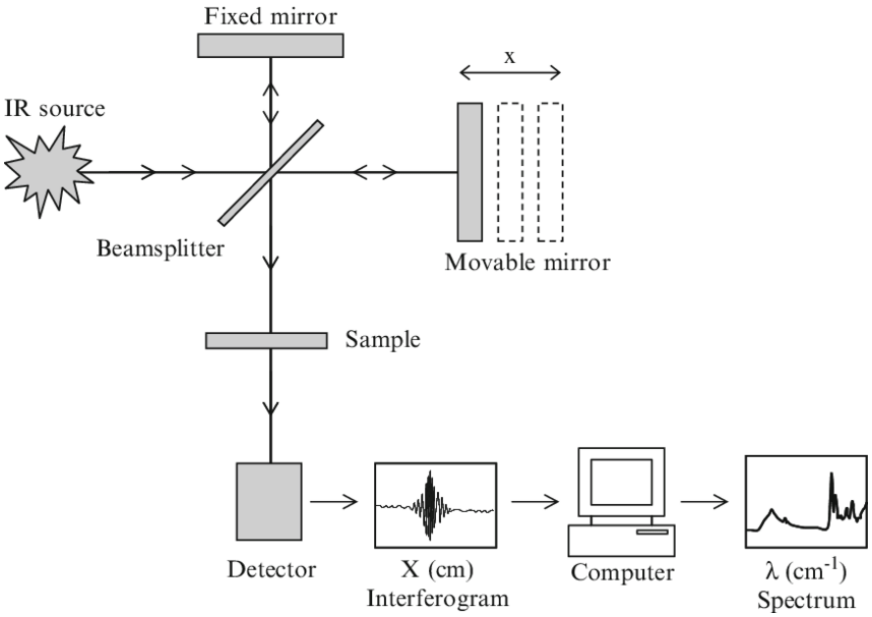


Figure 8: Schematic sketch of the essential features of a Fourier transform infrared (FTIR) spectrometer [65].

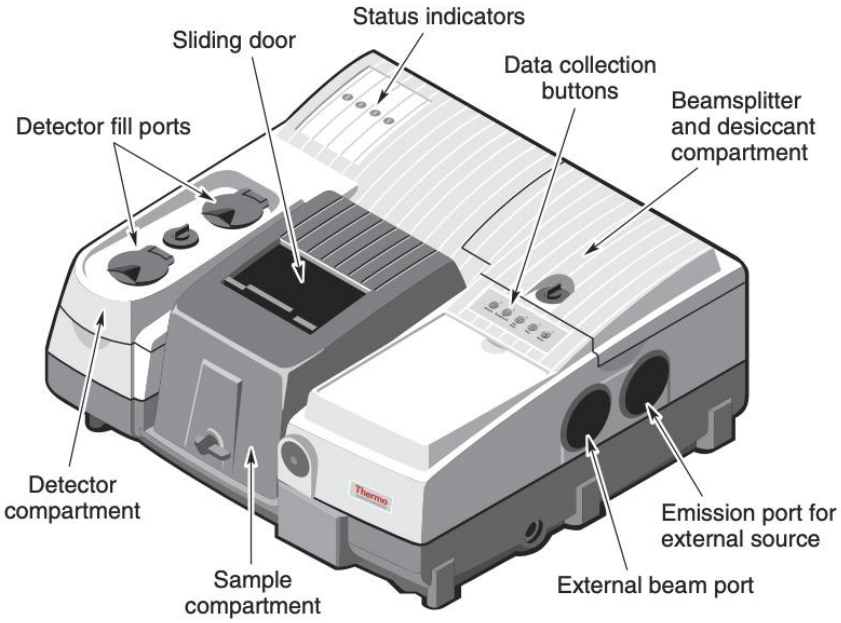


Figure 9: Nicolet 6700 spectrometer components [66].

However, there are also limitations to FTIR spectroscopy. For example, the technique is sensitive to the orientation and packing of molecules in the sample, which can affect the interpretation of

the spectra. FTIR is also susceptible to interference from water vapor and other atmospheric gases, which can obscure the spectra of interest [63]. Overall, FTIR spectra can provide information about the chemical composition, structure, and functional groups present in a sample, which can be used for identification, quantification, and quality control purposes.

3.4 Scanning Electron Microscope (SEM)

SEM is a type of microscope that uses a focused beam of electrons to create high-resolution images of the surface of solid objects. The highest quality SEMs are capable of producing images with a resolution of less than 1 nm, which is significantly better than the resolution achievable by even the most advanced optical microscopes, with a difference of several orders of magnitude [65]. SEM images are typically black and white, and they can reveal a great deal of detail about the surface structure and composition of a sample.

In an SEM, a beam of electrons is generated by an electron gun and focused onto a sample using a series of electromagnetic lenses (Fig. 10). As the electrons interact with the sample, they produce various signals that can be detected and used to create an image. These signals include secondary electrons (SEs), backscattered electrons (BSEs), and X-rays.

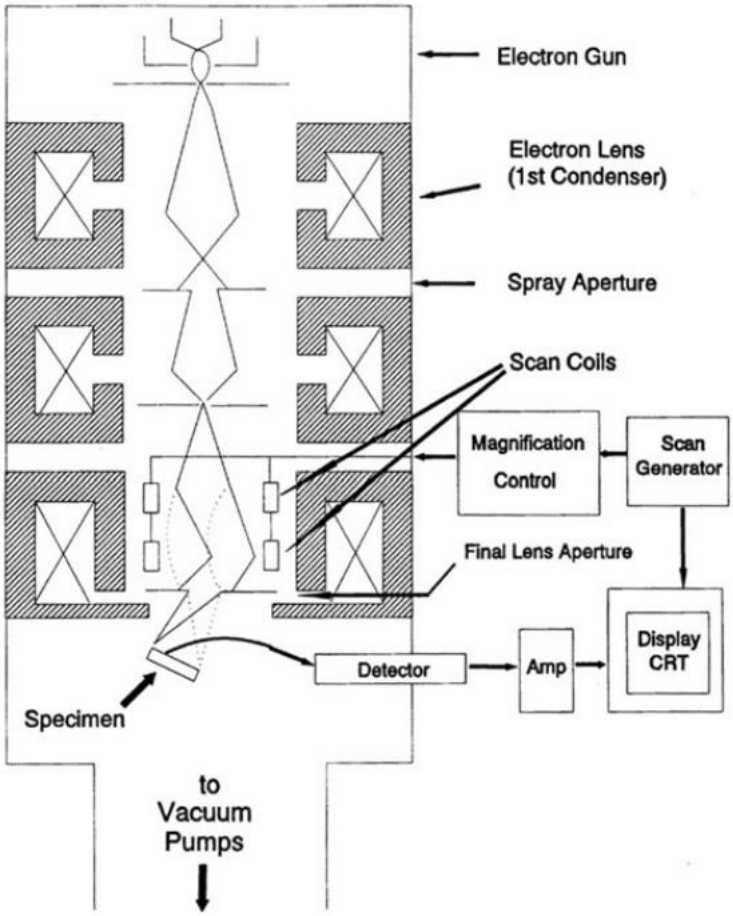


Figure 10: Schematic illustration of typical SEM setup [66].

The SE mode is widely used in SEM and can provide information about surface topography since it detects low-energy electrons (<50eV) that are emitted close to the sample's surface due to inelastic collisions with the electron beam generated by the gun [66]. These electrons, which originate from the surface layer of the sample, are useful for determining morphological and topographical information. On the other hand, BSEs are high-energy electrons that are initially emitted by the electron gun but are scattered back by the sample's electron cloud in elastic collisions. BSEs can be employed to quickly determine the material's phase composition. Elements with higher atomic numbers have denser electron clouds and backscatter more electrons, resulting

in a stronger signal and a brighter image. Conversely, elements with lower atomic numbers have less backscattering, leading to a weaker signal and a darker image.

3.5 Brunauer-Emmett- Teller (BET)

The BET method is a technique used to measure the surface area of solid materials, particularly porous materials such as catalysts, adsorbents, and powders. The BET method is based on the physical adsorption of gas molecules onto the surface of a solid material [67]. The technique involves measuring the amount of gas adsorbed at different pressures, typically using nitrogen gas as the adsorbate. The amount of gas adsorbed is related to the surface area of the material and can be used to calculate the specific surface area.

In this method, a sample of the material is first degassed to remove any adsorbed gases or moisture in the sample cell (Fig. 11). The sample is then placed in a chamber containing a gas, typically nitrogen, which is adsorbed onto the surface of the material. As the pressure of the gas is increased, more gas molecules are adsorbed onto the surface until a point of saturation is reached [68].

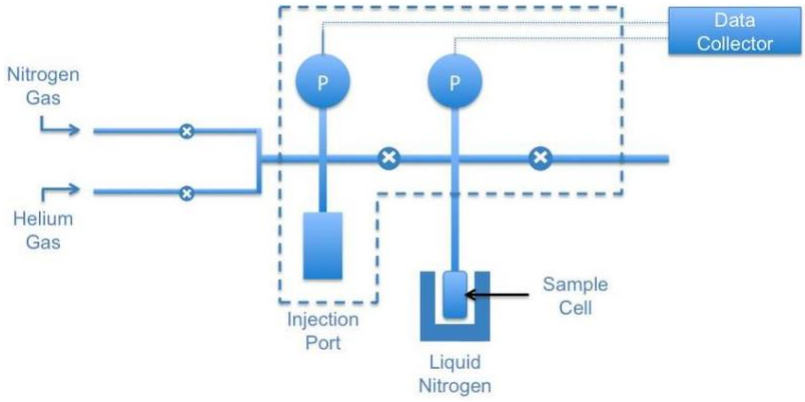


Figure 11: Schematic of BET surface analyzer [70].

The BET isotherm plot is a graph that shows the relationship between the amount of gas adsorbed by a solid material and the pressure of the gas at a constant temperature [69]. The BET isotherm is typically a sigmoidal curve with distinct regions that correspond to different types of adsorption (Fig. 12). At low pressures, the BET isotherm exhibits a linear region known as the monolayer region, where gas molecules are adsorbed one layer thick onto the surface of the material. As the pressure is increased, the amount of gas adsorbed increases, and the BET isotherm transitions into the multilayer region, where gas molecules begin to fill the pores of the material.

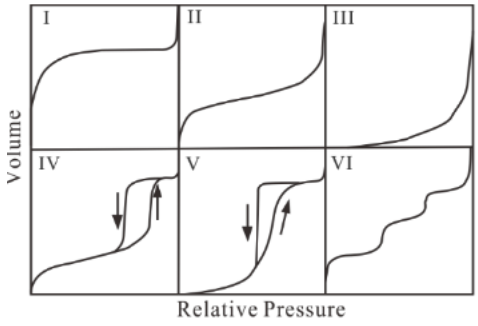


Figure 12: Types of adsorption isotherms [69].

The pore distribution plot is a graphical representation of the size distribution of pores within a material, based on the data obtained from the BET isotherm. The pore distribution plot typically shows the cumulative pore volume as a function of pore size, with different regions of the plot corresponding to different types of pores.

Finally, the BET method is a valuable technique for determining the porosity and surface area of a material, which can significantly impact its properties and potential applications. However, the BET method has certain limitations, including its assumption of uniform surface adsorption and its inability to differentiate between various pore types [69]. Additionally, the BET method

requires careful preparation and handling of samples, and the interpretation of data can be challenging and necessitates expertise in the field of materials science and chemistry.

3.6 Ultraviolet-Visible Spectroscopy (UV-vis)

UV-vis spectroscopy is a technique used to measure the absorption or transmission of light in the ultraviolet-visible region of the electromagnetic spectrum. The UV-vis spectrum can provide information about the electronic structure of molecules, as the absorption of light in this region is related to the energy required to excite electrons in molecules from one energy level to another. The amount of radiation that is transmitted through the sample is dependent on the concentration of the absorbing species, the path length of the sample, and the wavelength of the incident radiation [70].

The UV-vis spectrum of a sample is a plot of the amount of radiation absorbed or transmitted as a function of the wavelength of the incident radiation. The shape and intensity of the UV-vis spectrum are dependent on various factors, including the electronic structure of the sample, the solvent used, and the pH of the solution.

The basic setup of a UV-vis spectrophotometer includes a light source, monochromator, sample holder, and detector (shown in Fig. 13). The light source emits radiation in the UV-vis region, which passes through a monochromator to select a narrow range of wavelengths. The selected wavelengths pass through the sample holder containing the sample to be analyzed, where some radiation is absorbed and the rest is detected by the detector. Then detector converts the radiation into an electrical signal, which is processed and displayed as a UV-vis spectrum [70].

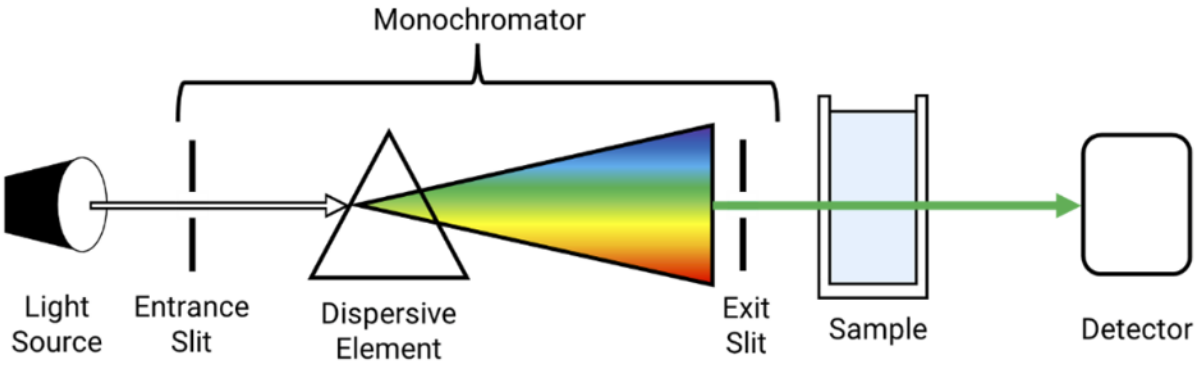


Figure 13: Basic block diagram of single beam UV-Vis spectrometer [71].

4.0 Evaluation of Different Graphene Manufacturing: Structure, Composition, and Electrochemical Properties

4.1 Introduction and Project purpose

Graphene owing to its unique features, such as the hardest honeycomb structure, large surface area and high conductivity, has been widely applied to the energy storage area. However, a comprehensive comparison of commonly used synthesis methods is still under study. On the one hand, most bulk-scale graphene is produced by a top-down approach, exfoliating graphite, which often requires large amounts of solvent and high-energy treatment. On the other hand, high-quality graphene produced by bottom-up methods is often restricted by the low yield of production.

This study focused on three highly promising methods for the synthesis of graphene: Hummer's method, chemical vapor deposition, and organic salts method. Due to the wide range of synthesis approaches available and their potential for commercialization, these three methods were chosen for investigation. The study involved producing HRGO and OSG materials in the lab and conducting tests to compare their physiochemical and electrochemical properties. However, the synthesis mechanism for CVD graphene requires specialized equipment and precise control of growth conditions, making it difficult to complete the procedure in the lab. Therefore, the study had to rely on experimental results from literature to compare CVD graphene with the other two approaches.

To evaluate the physiochemical property of the synthesized graphene and related materials (graphite and graphite oxide), various characterization methods were conducted, such as Raman, FTIR and BET surface area analysis. Finally, electrochemical performance will be discussed based on the results from the three-electrode system. Furthermore, the industrial application of graphene

from each synthesis method will be summarized to give a general outlook, which covers electronic devices and energy storage devices.

4.2 Experimental Section

4.2.1 Materials

All chemicals used in the following work were purchased from Sigma Aldrich and were used as raw material unless otherwise noted.

4.2.2 Hummer's Graphene (HRGO) Synthesis

rGO was prepared from GO synthesized by improved Hummer's method. The schematic is shown in Fig. 14. For the improved method, a mixture of H_2SO_4/H_3PO_4 (360:40 mL) was added to the commercial graphite powder (M2-15) in a flask and stirred for 30 mins in an ice bath. Add 18g $KMnO_4$ slowly with continuous stirring for 15 mins. The reaction has then raised the temperature to 50 ° C and stirred for 16 hours. Place the solution in the ice bath to cool down and add DDI water (400mL) drop by drop to the solution. After thoroughly mixing the solution, slowly add H_2O_2 (20mL, 30%) to the flask to start the reaction. For washing, distribute the solution evenly into centrifuge tubes and centrifuge for 10 mins at 8000 rpm. Disposed supernatant away, the remaining material was washed with DDI water, 210 mL HCl (30%), 200mL ethanol (50%), 210 mL HCl (5%) and 3X DDI water at 7000 rpm for 10 mins individually. The solid obtained was freeze-dried for 4 days to get 2g GO. Then, after thermal shock at 900 °C for 15 mins, GO can be completely converted to rGO [72].

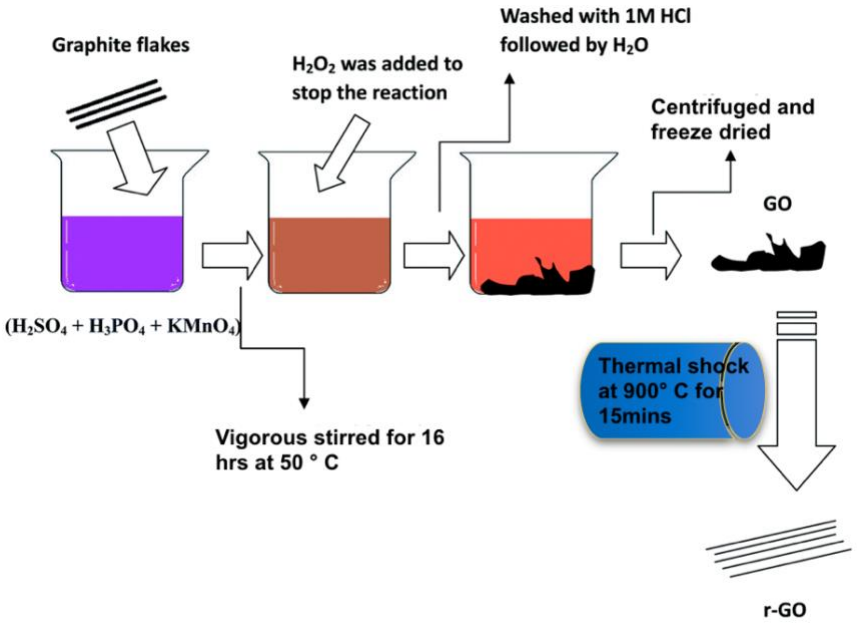


Figure 14: Schematic of Improved Hummer's Method.

4.2.3 Organic Salts Graphene (OSG) Synthesis

Few-layer graphene was prepared via a pyrolytic conversion method starting from mixing two salts (Fig. 15). Sodium citrate and sodium carbonate powder in a molar ratio of 5:20 were grounded for 30 mins using a mortar and pestle. The solid mixture was placed in a ceramic tube (1cm diameter) in a tube furnace. After flushing Ar in the system for 1 hour, the temperature started to raise to 950°C at a heating rate of 3°C·min^{-1} and held at this temperature for 10 mins. After cooling naturally under a flow of Ar, the resulting black powder was transferred to the beaker. Adding dilute HCl (2M) solution, the excess salts can be removed. To neutralize the solution, vacuum filtration with a nylon filter (0.45 µm) was performed using DDI water until reaching a neutral PH. The absolute ethanol (100 mL) was applied to remove the remaining water on the filter paper. Subsequent freeze-dry for 4 days yields pure few-layer graphene powder [13].

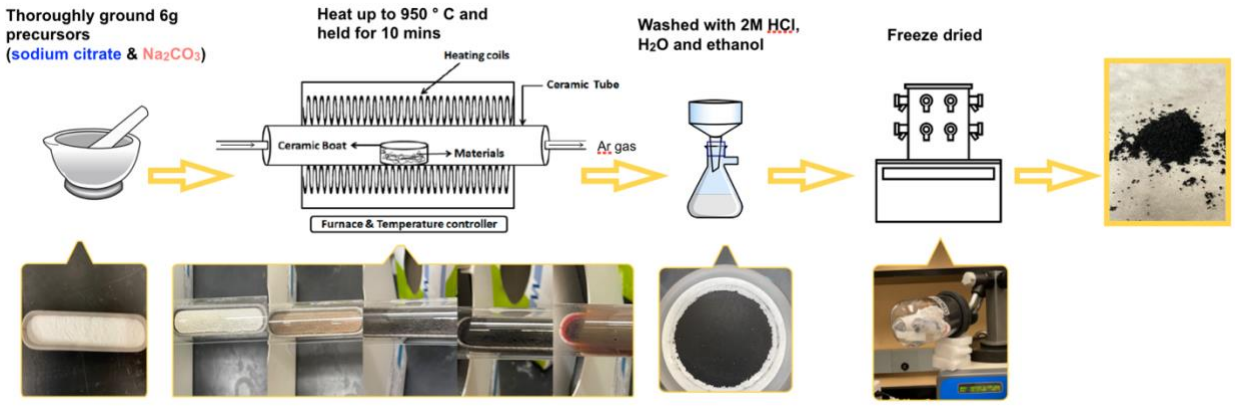


Figure 15: Schematic of Organic Salts method.

4.2.4 Material Characterization

The crystal structure of the carbon particles was analyzed using XRD on a Rigaku Miniflex 600 instrument with Cu-Kα radiation (λ = 1.542 Å). The defects and layer number of the graphene samples were studied through Raman spectroscopy (Bruker Senterra, 532 nm). The morphology of the powders was examined using SEM (Leo 1550, Zeiss). FTIR was performed using a Nicolet 6300, Thermo-Fisher with a resolution of 4 cm^{-1}. The surface area was evaluated through N2 adsorption-desorption isotherm analysis on a BET surface area analyzer (Quantachrome Instruments QuadraSorb SI4). The pore size distributions were determined based on the BJH model. The optical properties of the graphene were evaluated by performing UV-vis absorption spectroscopy and photoluminescence measurements using a monochromatic microplate spectrophotometer (Genesys 10S UV-vis).

4.2.5 Conductivity Test

The electrical conductivity of the infiltrated composites was determined during elongation by slicing the composites into small sheets and performing a 4-point probe test. A testing cell, designed and assembled in the laboratory and equipped with a modified stretching device, was used for the measurement of conductivity under strain. A simple schematic graph is shown in Fig.

16. The process began by mounting a sliced sample on the clamps of the stretching device, stretching the specimen, and fixing it in the elongated position. The fixed specimen was then placed in the 4-point probe testing cell to measure its conductivity while being elongated. The electrical conductivity was calculated by Eq. 5:

$$\sigma = \frac{1}{\rho} = \frac{1}{Rt} = \left(\frac{ln2}{\pi t}\right)\frac{I}{V} \qquad \textit{Equation 5}$$

where ρ is the electrical resistivity, R is the electrical resistance, t is the sample thickness, I is the applied current and V is the measured voltage drop [73].

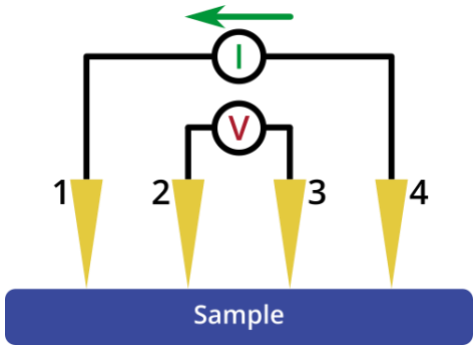


Figure 16: 4-point probe schematic view [74].

4.2.6 Electrochemical Characterization

The active electrode of the three-electrode system was obtained by mixing the organic salt graphene or hummer's graphene with super P and PVDF at a mass ratio of 8:1:1. With the help of DMF, the mixture was deposited onto Ni foil (1cm x 2cm) and subsequently dried overnight at 80 °C in a vacuum oven. The measurement was carried out in a three-electrode cell with a saturated Hg/HgO reference electrode, Graphene/Ni as a working electrode and a Pt plate as a counter electrode. A basic solution of slow-moving ions (2M KOH) was used as an electrolyte (as shown in Fig. 17). Cyclic voltammetry (CV) tests were performed in the potential range of -1 to -0.2 V. Galvanic charge-discharge (GCD) curves were carried out at various constant current densities. In

addition, electrochemical impedance spectroscopy (EIS) measurements were obtained using a potential amplitude of 200 mV in a range of frequencies from 200 kHz to 0.01 Hz. All electrochemical tests were performed at ambient conditions. The specific capacitance (Cs) was calculated from the CV curve using the following expression:

$$Cs = \frac{1}{2m \cdot \Delta V \cdot s} \int_{V_0}^{V_t} |i| dV \qquad \textit{Equation 6}$$

where ΔV is the potential window, m is the weight of the graphene material on the Ni foam, s is the scan rate or sweep rate and i is the current [75].

And for specific capacitance calculated from the GCD curve, Since *IR* drop is inevitable, one can adjust ΔV to exclude the *IR* drop for a more accurate result, i.e.,

$$C_T = \frac{I_{dis} \Delta t}{V_0 - V_{IRdrop}} \qquad \textit{Equation 7}$$

where I is the constant current, Δt is the charging or discharging time corresponding to the specified potential change ΔV[76].

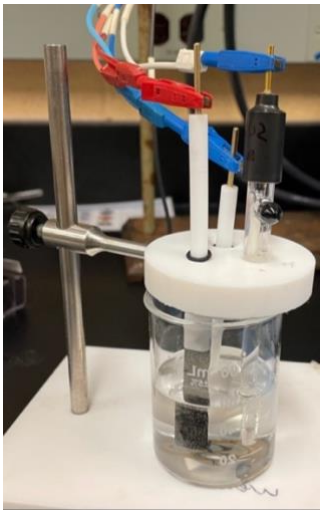


Figure 17: Three-electrode system.

4.3 Results and Discussion

X-Ray Diffraction (XRD) was used to characterize the graphitization of the amorphous carbon and measure the interlayer distance of carbon materials. The 2θ peak of a commercial graphite powder was at 26.6° (shown in Fig. 18a), with the interlayer distance of 3.35Å. Similarly, CVD graphene, OSG, and HRGO samples were detected that the (002) peak occurred at diffraction angle at 2θ =26.5°, 26.6° and 26.4° respectively, which corresponded to the graphite characteristic peak [77]. That confirms a successful graphitization of graphene materials. The interlayer distance for the three kinds of graphene (CVDG, OSG and HRGO) determined by Bragg's equation was calculated and summarized in Table 1 [58]. The interlayer distance of the C-C bond is larger and broader than the graphite result, especially for the OSG and HRGO. This difference is resulted from the well-ordered carbon structure and expanded 2D graphene sheets. After the introduction of oxygen, the peak at around 26.5° disappeared and contained only the distraction peak at 9.78°, showing it possessed only the sp^3 domain from the oxidized graphite domain. The increasing interlayer space of the GO sample (9.04 Å) suggests oxygen functional groups have been attached to the graphite lattice [78].

Table 1: Parameters extracted from the XRD spectrum of CVDG, HRGO, OSG, GO and commercial graphite.

Material ·	2θ (deg)	d-spacing (Å)	FWHM (rad)	Number of graphene Layers
Graphite	26.7	3.35	0.0039	14.5
GO	9.78	9.04	-	-
HRGO	27.1	4.03	0.0489	11.7
Graphene	26.6	3.35	0.158	3.5
CVD-G-Fe [77]	26.5	3.36	-	-

Raman spectroscopy has been the most direct way to capture the electronic structure of carbon materials. It excites a monochromatic laser and detects the characteristic of materials by identifying the vibrational modes [62]. In particular, it allows non-destructive and high-throughput identification of graphene layers and defects [79]. For comparison, the spectra result of commercial graphite and GO are included, which are raw materials used for producing RGO in Hummer's method. The Strokes phonon shift creates two main peaks in graphite samples: the G peak at ~1580 cm^{-1} as the primary in-plane vibration of sp^2 carbon and a band at ~2690 cm^{-1} named 2D, from the second order of zone-boundary phonons [60]. Besides, the D band usually observed at 1340 cm^{-1} is related to structural defects and disorder of the sp^2 carbon and domains [80]. After the oxidizing process, the D and G peaks in GO became sharper than the reduced GO, the 2D area was flatter as well. That is caused by the oxygen doping in graphene which shifts the Fermi level away and reduces the recombination possibility of excited photons [81][82]. The ratio of I_D/I_G of the HRGO was also lower compared to the GO, which has been commonly reported in the literature [83]. In this case of GO, the I_D/I_G ratio was 1.07 and after reduction, the ratio decreased to 1.02 (shown in Table 2). Among all three graphene, the G peak location was similar to the graphite result due to the first order of the E_{2g} mode, however, the intensity of the G peak was decreased from the top to bottom graphene samples in the Fig. 18b, which is relative to the crystallite size. The results indicated that HRGO sample reveals the lowest average crystallite size (L_a), 18.7 nm, followed by OSG (49.9 nm), and CVDG (128.2 nm) [38]. To be more specific, the average crystallite size of the sp^2 domains can be measured by the intensity ratio of D and G bands according to Cancodo et al. [78][61]. A lower crystalline size is due to the destruction of the crystalline structure resulting from the disorder and defects in the synthesis process. By combining the increased D peak and decreased 2D peak, CVD-produced graphene showed an outstanding uniformity lattice structure

and ordered crystal edges. Besides, based on the 2D shape and I_{2D}/I_G ratio, the quality of graphene can be distinguished by identifying the number of layers [1]. As shown in the graph, 2D peaks were shifted to the left with a decreased I_{2D}/I_G ratio for CVDG, OSG and HRGO. Meanwhile, the I_{2D}/I_G ratio of CVDG and OSG were calculated indicating the monolayer and few layers (tri-layers) structures respectively [84][85]. Thus, according to the Raman spectra result, it can be concluded that the CVD method and organic salt method produced graphene samples that demonstrated a well-ordered structure with fewer defects and layer numbers. These are the important parameters to consider the synthesized graphene to be developed and realized in practical applications.

Table 2: Parameters extracted from the Raman spectrum of CVDG, HRGO, OSG, GO and commercial graphite.

Material	Peak Location			I_D/I_G	I_{2D}/I_G	L_a
	D	G	2D			
Graphite	1338	1565	2694	0.089	0.416	215
GO	1339	1580	-	1.07	-	17.9
HRGO	1339	1580	-	1.028	-	18.7
OSG	1340	1570	2678	0.385	0.705	49.9
CVD-G-Ni[38]	1345	1565	2700	0.15	>1	128.2

In order to investigate the different types of functional groups on each graphene sample, FT-IR spectroscopy is used to obtain the absorbed/transmitted infrared radiation of materials [86]. Fig. 18c illustrates the spectra results for three types of graphene over the wavelength 600 cm^{-1} - 4000 cm^{-1}. Meanwhile, the spectra data of CVD graphene was tested on the Cu substrate. After subtracting the peak of the Cu substrate, no obvious functional groups were presented on CVD

graphene [87]. Apart from the absorbance band of CO_2 (2035 cm^{-1} - 2045 cm^{-1}) in air, there was a noise peak revealed at around 2700 cm^{-1} for HRGO and GO that can be assigned to mechanical vibration or environmental electrical effect. The respective functional group for each wavelength region has been labeled in Fig. 18c. Overall, it is proved that the synthesized graphene samples have been reduced successfully and shown no significant peak as same as the graphite result measured in literature [88][89] Upon oxidation, two prominent peaks appearing at 1780 cm^{-1} and 3450 cm^{-1} demonstrate an effective integration of carboxylic acid group (-COOH) and hydroxyl group (-OH).

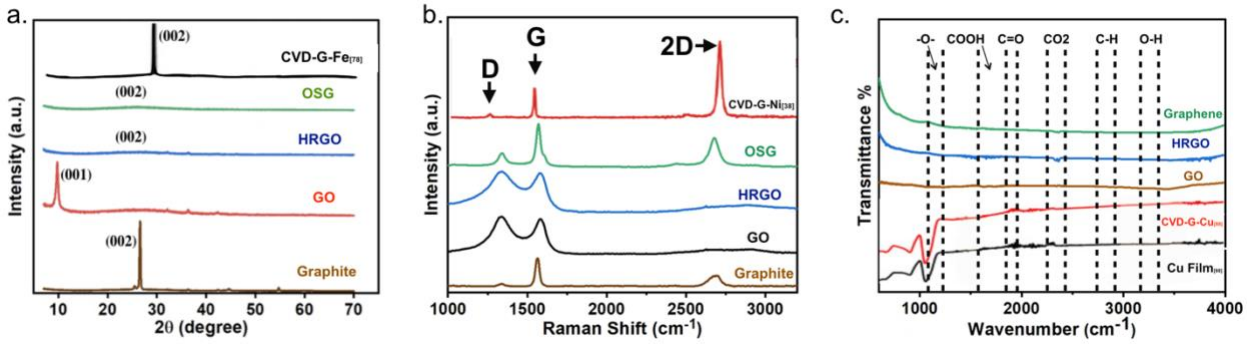


Figure 18: (a) XRD spectrum, (b) Raman Spectra, (c) FTIR spectra of CVDG, HRGO, OSG, GO and commercial graphite.

To visualize the morphology of graphene, SEM is widely used to capture the high-resolution picture of the material sample with applying a high-power electron source in the electron microscope. Fig. 19 (a-c) illustrates the few-layer graphene synthesized by organic salt precursor. After 950 °C pyrolysis process, the prepared graphene shown a 2D sheet structure indicates 100% successful conversion from sodium citrate precursor to 2D carbon nanostructure. In addition, highly sheer and flexible graphene sheets were observed in both OSG and HRGO (shown in Fig. 19 (d-f)). As compared to OSG, Hummer's graphene reveals a larger particle size at the same magnification level and tends to stack together. As related to the starting material, HRGO

synthesized from commercial graphite with a particle size of 15 mm has a larger particle size than OSG prepared from the ground salt precursors. Furthermore, graphene after APCVD process can be distinguished by the unique hexagonal structure and shown as the black area in Figure 19 (g-j) [90][91]. It demonstrates a controlled carbon nucleation and deposition process on Cu foil. The formed monolayer graphene contains fewer defects and is free of grain boundaries. A typical individual grain was captured under a high magnificent of 2 mm, representing an individual graphene crystalline with a flower-like four to six-lobed structure in a millimeter size [38].

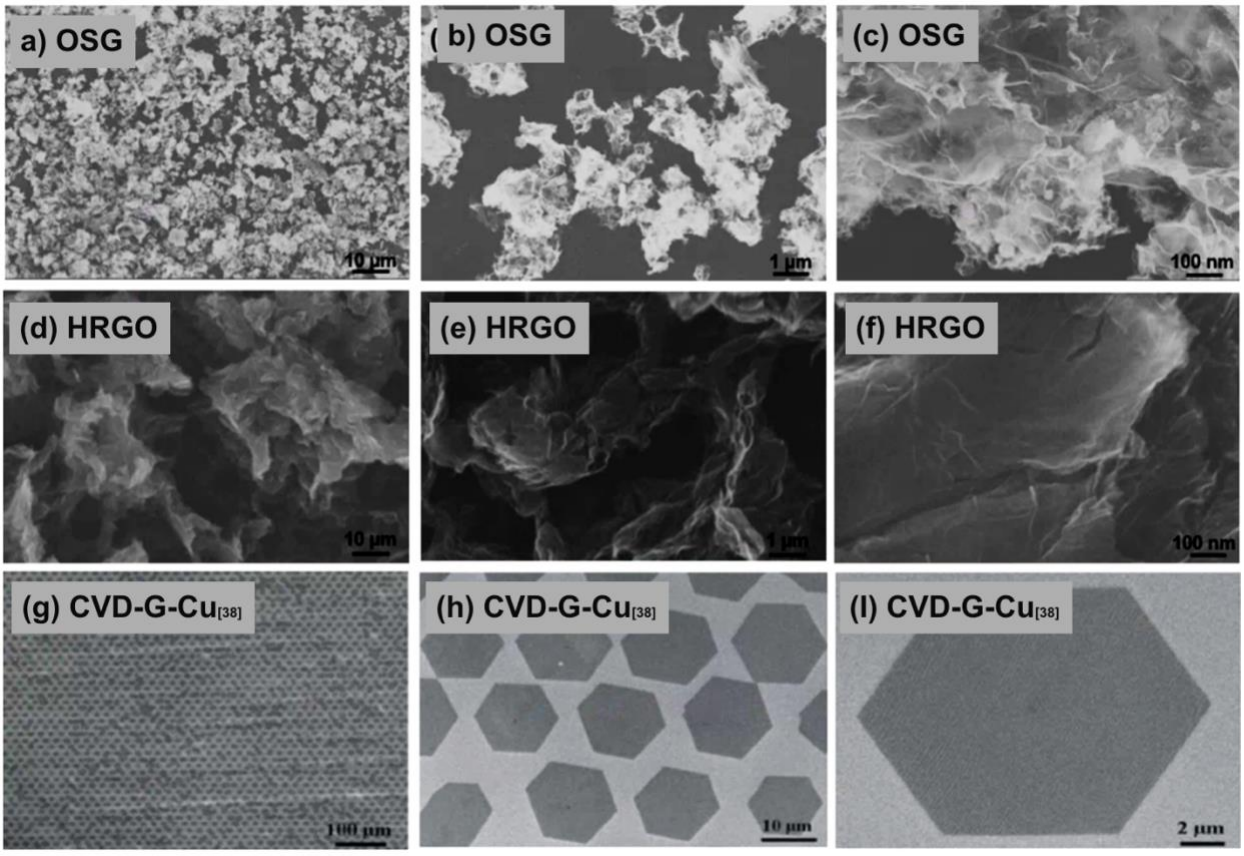


Figure 19: SEM images of OSG (a-c), HRGO (d-f) and CVD graphene (g-i).

The surface area of GO and graphene materials can be measured by BET analysis through nitrogen gas adsorption. Fig. 20 demonstrates the N_2 adsorption-desorption isotherms with hysteresis hoops and pore size distribution from 0-100 nm. From graphs a and b, a large amount of gas was adsorbed at very low pressure ($P/P_0 \sim 0$) indicates a micropore (<2nm) filling for GO and OSG. At lower pressure, the isotherm curve of OSG shows a shape of "knee" at 0.1 nm representing the few-layer structure which is consistent with the Raman result. Among all, the highest surface area (326.1 m^2/g) was detected for HRGO and more gas volume was adsorbed at high pressure. That implies mesopores (2-50 nm) and macropores (>50nm) contributed to more pore space in this case. In addition, the hysteresis loop comprised in the isotherm graph is used to identify the pore type of each material. For OSG, a long and wide H4-type loop is attributed to a parallel pore structure consisting of slit-shaped pores [69]. Due to the loose stacking of flaky particles in HRGO, wedge-shaped pores can be found from the outer boundary of the material which is also in agreement with the SEM result. Hence, the surface area of HRGO is significantly lower than the theoretical value of graphene produced by CVD method (2039 m^2/g) [92][93]. In addition, the pore size distribution graphs are shown in Fig. 20 (d-f), in which the vertical axis (dV/dlog(D)) denoted the rate of pore volume change with increased pore diameter. In particular, the dV/dlog(D) curve is continuously rising without a flat platform revealing that mesopores and macropores in the HRGO sample take more space. The pore volume is increased at the low diameter region for OSG and tends to be steady when the pore diameter approached to 7 nm. It is in line with the isotherm graph meaning that micropores and mesopores occupy a dominant position and increase the level of porosity.

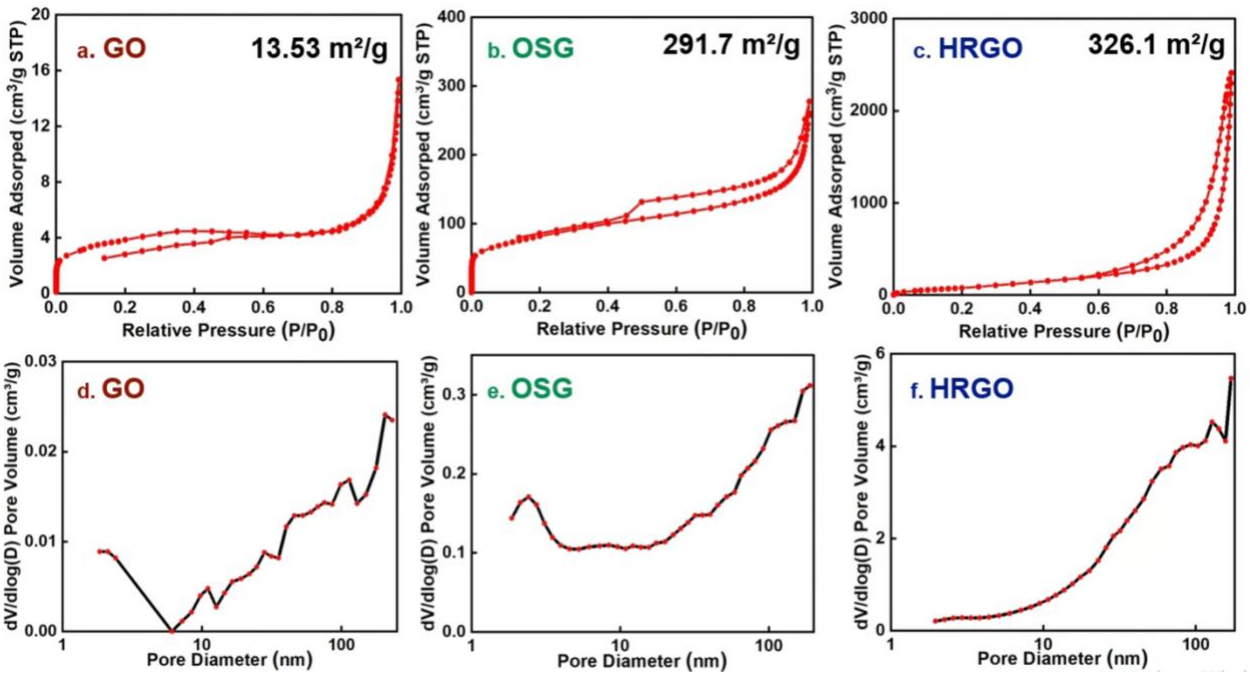


Figure 20: Nitrogen adsorption/desorption isothermals for (a) GO, (b) OSG and (c) HRGO; Pore size distribution of (d) GO, (e) OSG and (f) HRGO.

Fig. 21 shows the different behavior of equal amounts of OSG and HRGO dispersed in water for various duration. After sonification, HRGO slurry was in a more uniform status compared to OSG indicating a better dispersibility. That is probably due to the residual functional groups of GO remaining after thermal treatment. However, in contrast with HRGO which remained relatively stable, the OSG sample tends to aggregate together and more particles appeared on the top of the water level, indicating it is not completely dispersed in water. Hence, it concluded that HRGO is more hydrophilic and OSG is more hydrophobic. In addition, the spectroscopic and microscopic data analysis provided the identification and characterization of the dispersed material (as shown in Fig. 22). That suggests the graphene nanosheets have been successfully isolated and are present in a water suspension. The UV-Vis spectra of HRGO and OSG obtained from the analysis show a maximum wavelength around 380 nm and 350 nm, which is indicative of the π,π^* transition of the graphene. For HRGO, this transition starts to increase from 1100 nm and is a result of the

absorption of light by the graphene material. This also serves to indirectly confirm the homogeneity of the HRGO graphene nanosheets present in the water suspension. The analysis of the spectroscopic data provides insight into the electronic properties of the graphene nanosheets and is a crucial step in understanding their potential applications in various fields.

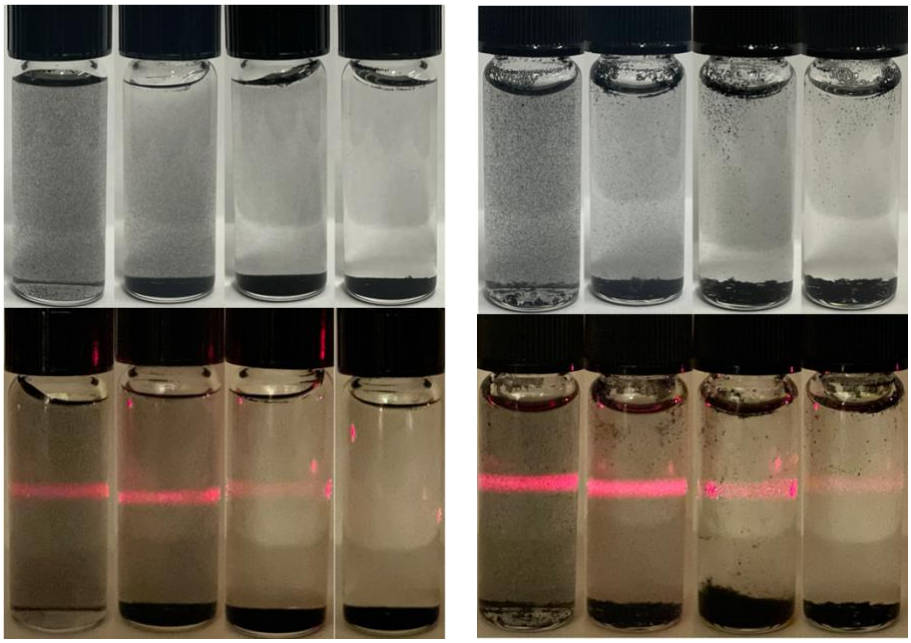


Figure 21: Dispersion test of HRGO (left), and OSG (right) at 0, 1, 5, 24 hours.

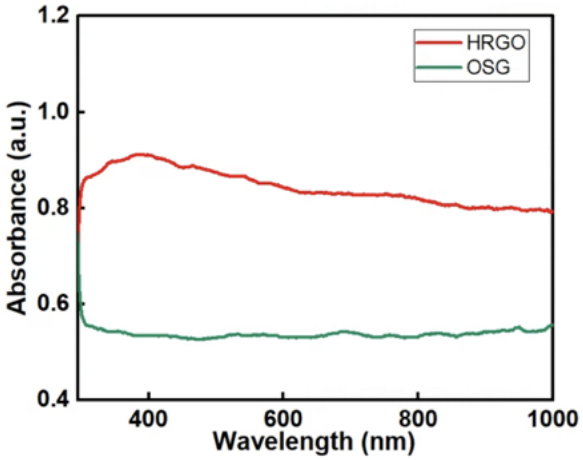


Figure 22: UV-vis absorption spectra of HRGO and OSG nanosheets dispersed in water.

Table 3 presents a summary of the results of in-plane DC electrical conductivity tests conducted on OSG, HRGO, and CVD-G. The findings indicate that CVD-G has the highest conductivity, with a theoretical value of 10^4 S/cm for an extremely thin monolayer CVD graphene [94]. The second-best conductivity was observed in OSG, which was tested using a uniformly pressed graphene disk. However, the conductivity of OSG was lower than that of CVD-G, as a thicker sample was used in the test. The morphology of the sample also played a role in the conductivity results [95]. The in-plane DC test used in the study has a unique feature where conduction is generated by an electron stream flowing at the surface above the percolating threshold [96]. Thereby decreasing the system discontinuity, the tested material OSG with a less structural defect and lower layer number, revealed a higher conductivity in comparison with HRGO. In addition, the study compared the results with commercially available reduced GO from Hummer's method, which has an electrical conductivity of 67 S/cm according to Graphenea [97]. This is slightly higher than the values reported in other literature, which typically range from 15-30 S/cm [98][99]. The difference in values could be attributed to variations in the conductivity setup used, as there is no information provided for the commercialized rGO. However, literature rGO used the same four-point probe method as the study did for HRGO, and a significant decrease in conductivity was observed. This was expected, as the degree of reduction, temperature, and atmospheric conditions can all affect the reduction procedure.

Table 3: Summary of Direct current conductivity results

Material	Thickness (cm)	Electrical Conductivity (in-plane DC) (S/cm)
OSG	0.0171	28.8
HRGO	0.0112	2.04
CVD-G[94]	-	$>10^4$

To investigate the ionic diffusion in graphene and electrochemical performance, cyclic voltammetry (CV), galvanic charge-discharge (GCD) and electrochemical impedance spectroscopy (EIS) measurement were performed in the alkaline electrolyte (2M KOH) in three-electrode setup, which usually yields a higher capacitance compared to the neutral electrolyte. A thin electrode was prepared by pasting a slurry of electrode material on Ni foam.

The CV curves at different scan rates from 1 to 20 mV/s are shown in Fig. 23 a and b. In Fig. 23 a, the CV curve of OSG is approximate a rectangle compared to HRGO, implying excellent double-layer electrical capacitance. And for HRGO, the inherent functional group on graphene surface generated during the synthesis procedure leads to pseudocapacitive behaviour. In this case, the charge storage mechanism is based on faradaic reactions (redox reactions) at the electrode-electrolyte interface. However, it appears that the HRGO demonstrated a larger enclosed area of CV curves than OSG, indicating a more significant capacitance improvement and better performance retention, especially at a higher scan rate. Similarly, results from GCD experiments at different current densities shared the same conclusion with the CV results. Fig. 23c, the GCD result for the OSG sample appeared a generally symmetric shape, emphasizing a sign of charge and discharge reversibility. The highest specific capacitance of OSG was calculated to be 93.77 F/g at the current density of 0.5 A/g. For HRGO, the discharge curve was observed a non-linear shape with a sudden IR drop at the beginning of discharge. Hence, the specific capacitance was derived and excluded IR drop for more accuracy. A much higher result was calculated from HRGO (144.2 F/g) at 0.5A/g as compared to OSG due to a large surface area and porosity that improve

the infiltration of electrolytes. The capacitance results are summarized in table 4 & 5 from the CV and GCD tests.

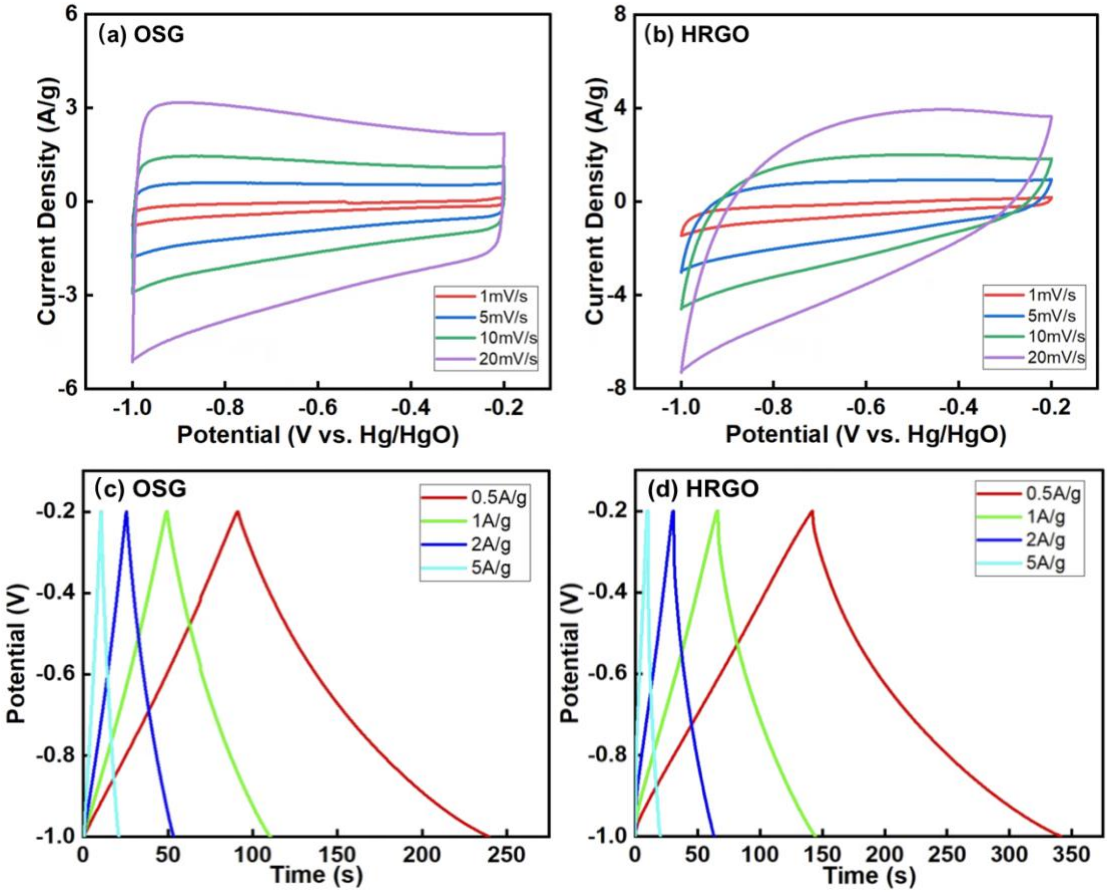


Figure 23: Represents (a-b) cyclic voltammetry curves, (c-d) galvanic charge-discharge curves of OSG (left), and HRGO (right).

Table 4: Summary of cyclic voltammetry results.

Scan rate (mV/s)	Capacitance (F/g)	
	OSG	HRGO
1	93.56	167.9
5	69.53	97.57
10	67.52	85.11
20	65.58	71.53

Table 5: Summary of galvanic charge-discharge (GCD) results.

Current Density (A/g)	Capacitance (F/g)	
	OSG	HRGO
0.5	93.77	144.2
1	77.13	97.34
2	70.25	92.25
5	65.52	80.93

The EIS data was assessed through a Nyquist plot to determine the internal resistance of the electrode and resistance between the electrode and electrolyte. The Nyquist plot (Fig. 24 a, b) was executed in the frequency range of 200 kHz to 0.01 Hz with a potential amplitude of 200 mV. In the Nyquist plot of OSG (Fig. 24 a), a nearly vertical line with a slight bend in the low-frequency region was observed, which indicates a typical capacitive performance. In the high frequency region, OSG-Ni electrode shows a more inconspicuous arc compared to HRGO, which represents a lower charge transfer resistance from solution to the graphene electrode. This is also agreed with the higher conductivity of OSG tested from a previous section. The intersection of the curve at the X-axis determines the equivalent series resistance (ESR) of the cell, which impacts the charging and discharging rate of the cell. The internal cell resistance (real Z' axis from Nyquist plot) was around 0.55 Ω for both graphene samples. The Warburg resistance, represented by the slope of the 45° portion of the curve, is caused by the frequency-dependent ion diffusion/transport in the electrolyte. The Warburg curve of HRGO was found to be shorter than the OSG supercapacitor electrodes, indicating that HRGO has a short ion diffusion path. This allows for efficient access of electrolyte ions to the graphene surface, as the electrolyte does not penetrate into the particulate.

In addition, a long-term cycling test was performed by repeating the GCD test at 200 kHz-10mHz for 10000 cycles. The relationship between discharge capacity and cycle number is shown in Fig. 24 c, d. With a more stable and long-lasting discharge performance, OSG was capable to maintain good stability till the end of cycles, due to a physical process of reversible adsorption and desorption of ions on the carbon electrode interface [100]. It was observed that the performance of HRGO decreased gradually over 10,000 cycles, with 89% retention. This reduction in performance is caused by a redox reaction between the surface of the electrode and the electrolyte. Therefore, the cyclic stability of the material is influenced by its functional groups as well as the presence of oxygen in the electrolyte.

Overall, HRGO exhibits a higher capacitance than OSG as indicated by its larger enclosed area of CV curves, demonstrating superior capacitance improvement and higher energy density. This can be attributed to HRGO's large surface area and porosity, which allow for accessible pathways for ion diffusion. The CV curve of OSG is approximately rectangular, indicating excellent double-layer electrical capacitance. On the other hand, HRGO has inherent functional groups on the graphene surface that cause pseudocapacitive behavior, which involves faradaic reactions at the electrode-electrolyte interface. From EIS results, OSG-Ni electrode showed lower electronic resistance between the graphene nanoparticles, which is agreed by high conductivity result from previous test. The Warburg curve of HRGO from EIS result was shorter than OSG, indicating a shorter ion diffusion path, which supports its superior capacitance. However, OSG exhibited better

cyclability and long-lasting discharge performance, while HRGO showed a drop in performance and 89% retention due to previous oxidation and structural defects detected by Raman test.

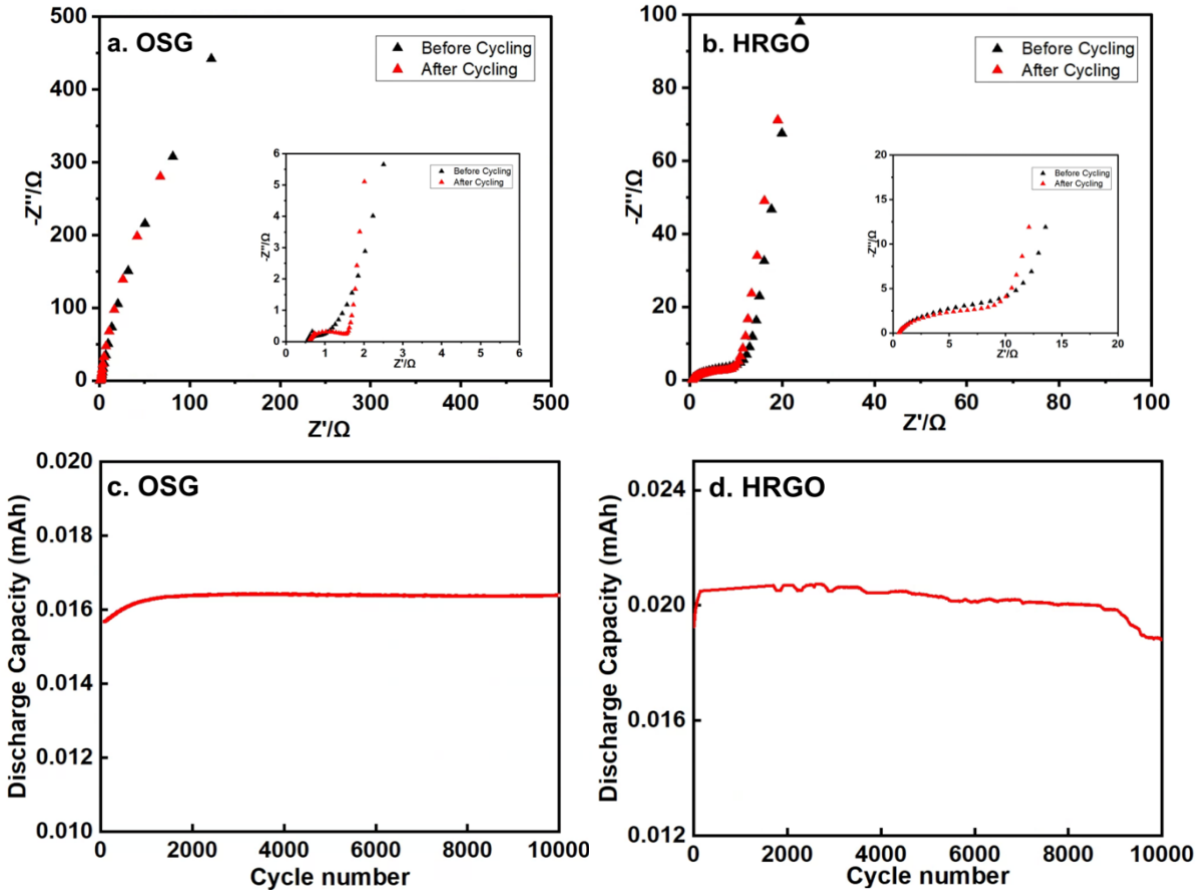


Figure 24: Represents (a-b) electrochemical impedance spectroscopy plot, (c-d)) Cyclability curves of OSG (the left) and HRGO (the right).

Moreover, it is crucial to consider a range of properties that are relevant to commercial applications, including material yield and production cost. Generally, CVD is a frequently employed technique to fabricate high-quality graphene on a substrate, although the produced graphene is in a very thin film format and is not free-standing, which significantly limits its practical industrial applications. In the CVD process, a carbon-containing gas (such as methane, acetylene, or ethanol) is utilized as the carbon source for graphene deposition. However, only a small proportion of the gas molecules are transformed into graphene, while the majority remain in their original form or

generate other by-products. The efficiency of gas source conversion into graphene is dependent on several factors, such as process conditions, gas source type and purity, and equipment quality, and can range from a few percent to approximately 50%. Additionally, the production cost of CVD graphene can vary depending on various factors, including equipment cost, raw material cost, and labor cost. Generally, the production cost can range from several hundred to several thousand dollars per square meter, depending on the production scale and the quality of the resulting graphene.

The yield of graphene produced through the organic salts method largely depends on the reaction conditions. In order to optimize the yield, various parameters are adjusted during the experiment such as grinding time, protection gas flow rate, ramping rate, and holding temperature. With appropriate adjustments to these parameters, a yield of around 15% can be achieved using the organic salts method. This is lower than the yield achieved with Hummer's method, which can reach up to 25-35%.

Despite the lower yield, the organic salts method offers advantages in terms of cost. The method uses common salt reactants that are inexpensive and widely available, and the procedure is relatively simple compared to other methods. This results in a lower overall cost, including material cost, labor, equipment, and electrical costs.

Another advantage of the organic salts method is that the synthesized graphene is in powder form, which is widely accepted in many different application scenarios. This is because the powder can be easily transformed into various formats, such as slurry, film, hydrogel, and foam, making it

versatile for different applications. Overall, while the yield of the organic salts method may be lower than other methods, its cost-effectiveness and versatility make it an attractive option for graphene synthesis.

As we know the application direction of a material is commonly related to its properties. Therefore, it is crucial to find out the specific demands for each industrial field. A summary and comparison of the important features and corresponding commercial application is shown in Table 6.

Table 6: A summary of the significant properties of for various applications.

	Material form	Less layer required	Electrical conductivity	Strength	Elasticity	Surface area	Thermal conductivity
Energy Storage device	Powder/flake		√			√	
Transistors	Film	√	√				
Conductive films & inks	Film/powder/flake	√	√		√		
Polymer composites	Powder/flake	√	√	√	√	√	√
Sensors	Film/powder	√	√				

5.0 Summary

The success of commercializing graphene products relies on the efficient industrial production of graphene, with a focus on factors such as quality, cost, consistency, ease of processing, and safety. The transition from laboratory-scale production to industrialization is not a straightforward process and new challenges emerge at each step. Hence, it's crucial to assess the properties of each graphene synthesis method and determine the most suitable method for each industry. The previous tests access the different types of graphene based on their properties, such as defect density, electrical conductivity, surface area, layer number, yield and cost.

As depicted in Fig. 25, the CVD process has proven to be highly effective in producing graphene films of exceptional quality, with a low density of defects and a high surface area. With the addition of advanced substrate substitution techniques, it is now possible to easily grow and transfer graphene films onto desired surfaces. Whereas, the limitations of CVD include high production costs, limited scalability, difficulty in controlling the quality of graphene, and the need for specialized equipment. In comparison with the traditional bottom-up methods, graphene powder synthesized by OSG possesses a more uniform graphene with less density of defects and layer number. Owing to the reversible reaction process and reductive intermediate products, it is also possible to control the interlayer distance and layer number of the resultant graphene. That is beneficial to satisfy the demands from different kinds of customers. Although it has a relatively low yield, the budget-friendly material and operation costs provide the commercial companies with possibility to satisfy the scale up requirements. Similarly, Hummer's method is also able to control over graphene properties. By regulating the degree of oxidation and exfoliation, researchers can produce graphene with different properties, such as size, thickness, and electrical

conductivity. Moreover, this method is scalable, meaning that it can produce large quantities of graphene oxide. This characteristic is essential for industrial applications where large amounts of graphene are required. Additionally, the materials used in the Hummer's method are relatively inexpensive, making it a cost-effective method for graphene production. However, the Hummer's method also has some weaknesses. One of the significant concerns is environmental issues. The process involves the use of strong oxidizing agents such as concentrated sulfuric acid and potassium permanganate, which can cause environmental pollution if not disposed of properly. The process is also time-consuming, with oxidation and exfoliation steps taking several hours each, which can affect the overall efficiency of the method. Another weakness is that the harsh chemical treatment used in the Hummer's method can cause defects in the graphene structure, leading to a high defect density. These defects can negatively impact the graphene's properties, such as mechanical strength, thermal conductivity, and electrical conductivity, limiting its practical applications.

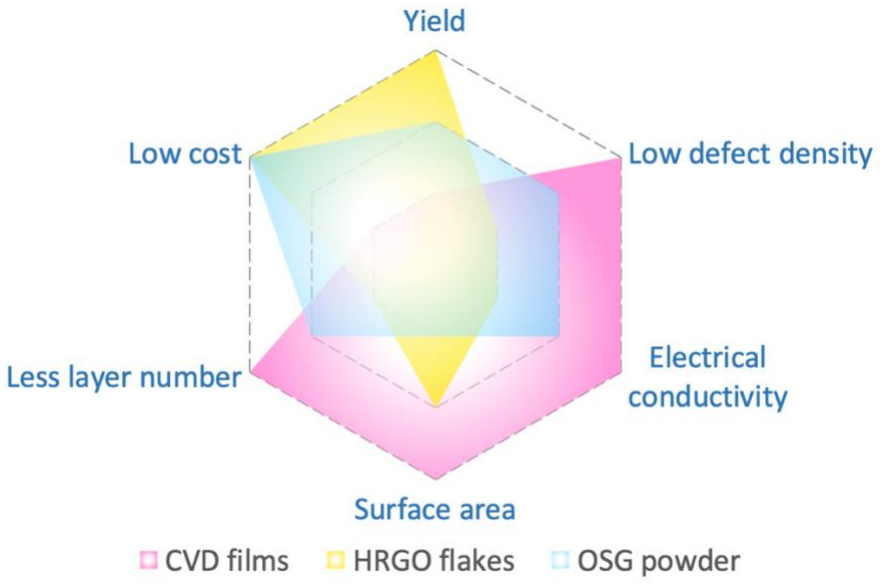


Figure 25: An evaluation of various graphene and derivative products, considering the intrinsic properties based on yield, defect density, electrical conductivity, surface area, layer number, and cost. The ranking of low, medium, and high levels is represented by the number 1, 2, 3 respectively.

6.0 Outlook

To provide valuable perspective for different application areas, we combined Table 6 and Figure 25 to generate a summary graph allocated the three most representative synthesis method to different industry area, as shown in Fig. 26. Along with the specialized needs for different industrial products, the high quality and low defect features make CVD film an ideal choice as a material for sensors and transistors. Moreover, CVD graphene is a material that is atomically thin, leading to low capacitance and low power consumption. This makes it ideal for use in low-power, high-frequency applications such as radio frequency communication and high-speed computing. In addition, for organic salts graphene powder with a lower number of layers is able to exhibit high electrocatalytic activity, making it an attractive material for use in these devices. In addition, graphene powder with a low cost also shows great potential in large scale energy storage applications. At the same time, it has a large surface area, which is beneficial for applications such as supercapacitors, where high surface area is important for high energy storage capacity. Hummer's graphene have been proved to apply in a range of industry scenario, including coatings and polymer composites. By leveraging the unique properties of graphene, these coatings offer improved performance and longer life compared to traditional coatings. Besides, graphene powder can be used as a reinforcement material in polymer composites to improve their mechanical, thermal, and electrical properties. However, this process often results in graphene with a large number of defects and a relatively low degree of crystallinity, which can impact the performance in applications such as electronics.

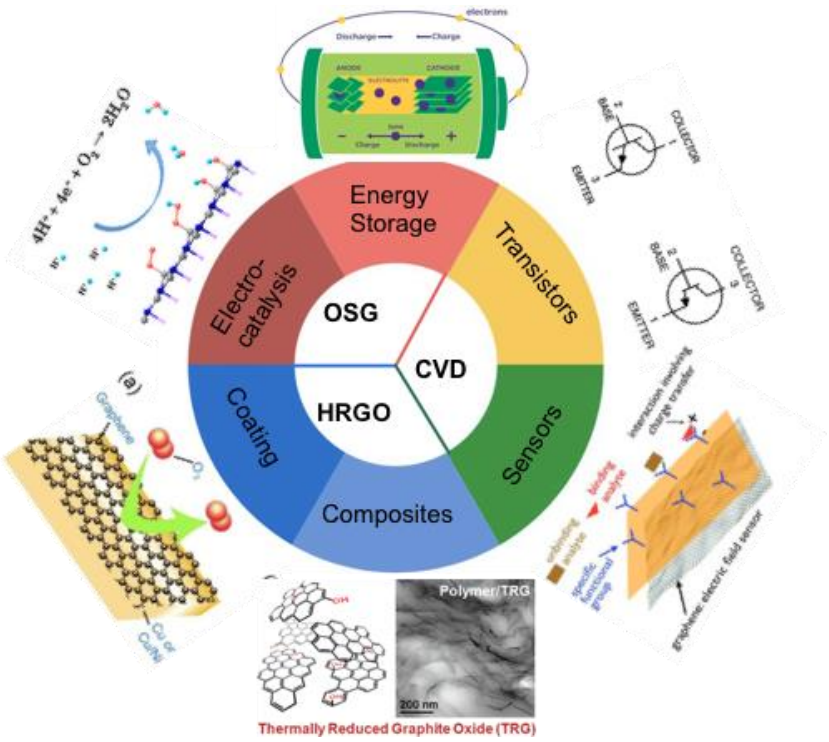


Figure 26: A diagram displaying various graphene synthesis method and some of their eventual applications.

Reference

[1] Y. Zhu *et al.*, “Graphene and graphene oxide: Synthesis, properties, and applications,” *Adv. Mater.*, vol. 22, no. 35, pp. 3906–3924, 2010, doi: 10.1002/adma.201001068.

[2] T. Barkan, “Graphene: the hype versus commercial reality,” *Nat. Nanotechnol.*, vol. 14, no. 10, pp. 904–906, 2019, doi: 10.1038/s41565-019-0556-1.

[3] C. Lee, X. Wei, J. W. Kysar, and J. Hone, “Measurement of the elastic properties and intrinsic strength of monolayer graphene,” *Science (80-.).*, vol. 321, no. 5887, pp. 385–388, 2008, doi: 10.1126/science.1157996.

[4] R. R. Nair *et al.*, “Fine structure constant defines visual transparency of graphene,” *Science (80-.).*, vol. 320, no. 5881, p. 1308, 2008, doi: 10.1126/science.1156965.

[5] M. Orlita *et al.*, “Approaching the dirac point in high-mobility multilayer epitaxial graphene,” *Phys. Rev. Lett.*, vol. 101, no. 26, pp. 1–4, 2008, doi: 10.1103/PhysRevLett.101.267601.

[6] A. K. Geim and K. S. Novoselov, “The rise of graphene PROGRESS,” *Nat. Mater.*, vol. 6, no. 3, pp. 183–191, 2007.

[7] S. H. Choi *et al.*, “Large-scale synthesis of graphene and other 2D materials towards industrialization,” *Nat. Commun.*, vol. 13, no. 1, pp. 1–5, 2022, doi: 10.1038/s41467-022-29182-y.

[8] Y. Zhu, H. Ji, H. M. Cheng, and R. S. Ruoff, “Mass production and industrial applications of graphene materials,” *Natl. Sci. Rev.*, vol. 5, no. 1, pp. 90–101, 2018, doi: 10.1093/nsr/nwx055.

[9] L. Lin, H. Peng, and Z. Liu, “Synthesis challenges for graphene industry,” *Nat. Mater.*, vol. 18, no. 6, pp. 520–524, 2019, doi: 10.1038/s41563-019-0341-4.

[10] I. Vlassiouk *et al.*, “Large scale atmospheric pressure chemical vapor deposition of graphene,” *Carbon N. Y.*, vol. 54, pp. 58–67, 2013, doi: 10.1016/j.carbon.2012.11.003.

[11] S. Bae *et al.*, “Roll-to-roll production of 30-inch graphene films for transparent electrodes,” *Nat. Nanotechnol.*, vol. 5, no. 8, pp. 574–578, 2010, doi: 10.1038/nnano.2010.132.

[12] M. Choucair, P. Thordarson, and J. A. Stride, “Gram-scale production of graphene based on solvothermal synthesis and sonication,” *Nat. Nanotechnol.*, vol. 4, no. 1, pp. 30–33, 2009, doi: 10.1038/nnano.2008.365.

[13] Y. Zhu, T. Cao, C. Cao, X. Ma, X. Xu, and Y. Li, “A general synthetic strategy to monolayer graphene,” *Nano Res.*, vol. 11, no. 6, pp. 3088–3095, 2018, doi: 10.1007/s12274-017-1703-3.

[14] “End-of-life F-150 Trucks Get Flashy Plastic-to-Graphene Treatment.” .

[15] P. T. Araujo, M. Terrones, and M. S. Dresselhaus, “Defects and impurities in graphene-like materials,” *Mater. Today*, vol. 15, no. 3, pp. 98–109, 2012, doi: 10.1016/S1369-7021(12)70045-7.

[16] E. Peng, N. Todorova, and I. Yarovsky, “Effects of Size and Functionalization on the Structure and Properties of Graphene Oxide Nanoflakes: An in Silico Investigation,” *ACS Omega*, vol. 3, no. 9, pp. 11497–11503, 2018, doi: 10.1021/acsomega.8b00866.

[17] H. C. Lee *et al.*, “Review of the synthesis, transfer, characterization and growth mechanisms of single and multilayer graphene,” *RSC Adv.*, vol. 7, no. 26, pp. 15644–15693, 2017, doi: 10.1039/C7RA00392G.

[18] W. H. Hale, “American Association for the Advancement of Science,” *Sci. Am.*, vol. 75, no. 1933supp, pp. 34–34, 1913, doi: 10.1038/scientificamerican01181913-34supp.

[19] S. Das Sarma, S. Adam, E. H. Hwang, and E. Rossi, “Electronic transport in two-dimensional graphene,” *Rev. Mod. Phys.*, vol. 83, no. 2, pp. 407–470, 2011, doi: 10.1103/RevModPhys.83.407.

[20] M. Yi and Z. Shen, “A review on mechanical exfoliation for the scalable production of graphene,” *J. Mater. Chem. A*, vol. 3, no. 22, pp. 11700–11715, 2015, doi: 10.1039/c5ta00252d.

[21] R. Jha, A. Singh, P. K. Sharma, O. Porwal, and N. K. Fuloria, *Graphene-based nanomaterial system: a boon in the era of smart nanocarriers*, vol. 51, no. 3. Springer Singapore, 2021.

[22] Y. Huang *et al.*, “Reliable Exfoliation of Large-Area High-Quality Flakes of Graphene and Other Two-Dimensional Materials,” *ACS Nano*, vol. 9, no. 11, pp. 10612–10620, 2015, doi: 10.1021/acsnano.5b04258.

[23] Q. Abbas *et al.*, “Graphene Synthesis Techniques and Environmental Applications,” *Materials (Basel).*, vol. 15, no. 21, 2022, doi: 10.3390/ma15217804.

[24] Y. Hernandez *et al.*, “High-yield production of graphene by liquid-phase exfoliation of graphite,” *Nat. Nanotechnol.*, vol. 3, no. 9, pp. 563–568, 2008, doi: 10.1038/nnano.2008.215.

[25] A. B. Bourlinos, V. Georgakilas, R. Zboril, T. A. Sterioti, and A. K. Stubos, “Liquid-Phase Exfoliation of Graphite Towards Solubilized Graphenes,” *Small*, vol. 5, no. 16, pp. 1841–1845, 2009, doi: 10.1002/smll.200900242.

[26] Z. Y. Xia *et al.*, “The exfoliation of graphene in liquids by electrochemical, chemical, and sonication-assisted techniques: A nanoscale study,” *Adv. Funct. Mater.*, vol. 23, no. 37, pp. 4684–4693, 2013, doi: 10.1002/adfm.201203686.

[27] K. Parvez, S. Yang, X. Feng, and K. Müllen, “Exfoliation of graphene via wet chemical routes,” *Synth. Met.*, vol. 210, pp. 123–132, 2015, doi: 10.1016/j.synthmet.2015.07.014.

[28] K. Parvez *et al.*, “Exfoliation of graphite into graphene in aqueous solutions of inorganic salts,” *J. Am. Chem. Soc.*, vol. 136, no. 16, pp. 6083–6091, 2014, doi: 10.1021/ja5017156.

[29] R. R. May *et al.*, “On the Atomic Weight o f Graphite. JBy,” *J. Hazard. Mater.*, vol. 338, no. 5, pp. 1677–1695, 2012.

[30] A. Ambrosi, C. K. Chua, A. Bonanni, and M. Pumera, “Electrochemistry of graphene and related materials,” *Chem. Rev.*, vol. 114, no. 14, pp. 7150–7188, 2014, doi: 10.1021/cr500023c.

[31] M. J. McAllister *et al.*, “Single sheet functionalized graphene by oxidation and thermal expansion of graphite,” *Chem. Mater.*, vol. 19, no. 18, pp. 4396–4404, 2007, doi: 10.1021/cm0630800.

[32] and J. H. . F. Nicholas A . Kotov, Imre DPkriny, “Ultrathin graphite oxide–polyelectrolyte composites prepared by self-assembly Transition,” *Adv. Mater.*, vol. 8, no. 8, pp. 637–641, 1996.

[33] S. Stankovich *et al.*, “Synthesis of graphene-based nanosheets via chemical reduction of exfoliated graphite oxide,” *Carbon N. Y.*, vol. 45, no. 7, pp. 1558–1565, 2007, doi: 10.1016/j.carbon.2007.02.034.

[34] L. J. Cote, R. Cruz-Silva, and J. Huang, “Flash reduction and patterning of graphite oxide and its polymer composite,” *J. Am. Chem. Soc.*, vol. 131, no. 31, pp. 11027–11032, 2009, doi: 10.1021/ja902348k.

[35] V. Strong *et al.*, “Patterning and electronic tuning of laser scribed graphene for flexible all-carbon devices,” *ACS Nano*, vol. 6, no. 2, pp. 1395–1403, 2012, doi:

10.1021/nn204200w.

[36] J. K. Wassei *et al.*, “Chemical vapor deposition of graphene on copper from methane, ethane and propane: Evidence for bilayer selectivity,” *Small*, vol. 8, no. 9, pp. 1415–1422, 2012, doi: 10.1002/smll.201102276.

[37] P. R. Somani, S. P. Somani, and M. Umeno, “Planer nano-graphenes from camphor by CVD,” *Chem. Phys. Lett.*, vol. 430, no. 1–3, pp. 56–59, 2006, doi: 10.1016/j.cplett.2006.06.081.

[38] R. Muñoz and C. Gómez-Aleixandre, “Review of CVD synthesis of graphene,” *Chem. Vap. Depos.*, vol. 19, no. 10–12, pp. 297–322, 2013, doi: 10.1002/cvde.201300051.

[39] A. Adetayo and D. Runsewe, “Synthesis and Fabrication of Graphene and Graphene Oxide: A Review,” *Open J. Compos. Mater.*, vol. 09, no. 02, pp. 207–229, 2019, doi: 10.4236/ojcm.2019.92012.

[40] Y. Hao *et al.*, “The role of surface oxygen in the growth of large single-crystal graphene on copper,” *Science (80-.).*, vol. 342, no. 6159, pp. 720–723, 2013, doi: 10.1126/science.1243879.

[41] X. Liang *et al.*, “ACS NANO 2011, 5 (11) 9144.pdf,” no. 11, pp. 9144–9153, 2011.

[42] X. Yan, “2018_Pnas_Si_Spe,” *Proc. Natl. Acad. Sci.*, vol. 120, no. 44, p. 2017, 2017, doi: 10.1073/pnas.

[43] A. Ambrosi, A. Bonanni, Z. Sofer, and M. Pumera, “Large-scale quantification of CVD graphene surface coverage,” *Nanoscale*, vol. 5, no. 6, pp. 2379–2387, 2013, doi: 10.1039/c3nr33824j.

[44] J. P. Naik, P. Sutradhar, and M. Saha, “Molecular scale rapid synthesis of graphene quantum dots (GQDs),” *J. Nanostructure Chem.*, vol. 7, no. 1, pp. 85–89, 2017, doi:

10.1007/s40097-017-0222-9.

[45] X. Yan, X. Cui, and L. S. Li, “Synthesis of large, stable colloidal graphene quantum dots with tunable size,” *J. Am. Chem. Soc.*, vol. 132, no. 17, pp. 5944–5945, 2010, doi: 10.1021/ja1009376.

[46] R. Liu, D. Wu, X. Feng, and K. Müllen, “Bottom-up fabrication of photoluminescent graphene quantum dots with uniform morphology,” *J. Am. Chem. Soc.*, vol. 133, no. 39, pp. 15221–15223, 2011, doi: 10.1021/ja204953k.

[47] J. Lu, P. S. E. Yeo, C. K. Gan, P. Wu, and K. P. Loh, “Transforming C 60 molecules into graphene quantum dots,” *Nat. Nanotechnol.*, vol. 6, no. 4, pp. 247–252, 2011, doi: 10.1038/nnano.2011.30.

[48] L. Tang *et al.*, “Deep ultraviolet photoluminescence of water-soluble self-passivated graphene quantum dots,” *ACS Nano*, vol. 6, no. 6, pp. 5102–5110, 2012, doi: 10.1021/nn300760g.

[49] Y. Dong *et al.*, “Blue luminescent graphene quantum dots and graphene oxide prepared by tuning the carbonization degree of citric acid,” *Carbon N. Y.*, vol. 50, no. 12, pp. 4738–4743, 2012, doi: 10.1016/j.carbon.2012.06.002.

[50] S. Chahal, N. Yousefi, and N. Tufenkji, “Green Synthesis of High Quantum Yield Carbon Dots from Phenylalanine and Citric Acid: Role of Stoichiometry and Nitrogen Doping,” *ACS Sustain. Chem. Eng.*, vol. 8, no. 14, pp. 5566–5575, 2020, doi: 10.1021/acssuschemeng.9b07463.

[51] J. Wu, W. Pisula, and K. Mu, “Wu+07Cr,” pp. 1–30, 2007.

[52] L. Jiao, L. Zhang, X. Wang, G. Diankov, and H. Dai, “Narrow graphene nanoribbons from carbon nanotubes,” *Nature*, vol. 458, no. 7240, pp. 877–880, 2009, doi:

10.1038/nature07919.

[53] D. V. Kosynkin *et al.*, “Longitudinal unzipping of carbon nanotubes to form graphene nanoribbons,” *Nature*, vol. 458, no. 7240, pp. 872–876, 2009, doi: 10.1038/nature07872.

[54] B. Genorio, Z. Peng, W. Lu, B. K. Price Hoelscher, B. Novosel, and J. M. Tour, “Synthesis of dispersible ferromagnetic graphene nanoribbon stacks with enhanced electrical percolation properties in a magnetic field,” *ACS Nano*, vol. 6, no. 11, pp. 10396–10404, 2012, doi: 10.1021/nn304509c.

[55] C. Hong An Wong and M. Pumera, “Unscrolling of multi-walled carbon nanotubes: Towards micrometre-scale graphene oxide sheets,” *Phys. Chem. Chem. Phys.*, vol. 15, no. 20, pp. 7755–7759, 2013, doi: 10.1039/c3cp51026c.

[56] C. K. Chua, Z. Sofer, and M. Pumera, “Graphene sheet orientation of parent material exhibits dramatic influence on graphene properties,” *Chem. - An Asian J.*, vol. 7, no. 10, pp. 2367–2372, 2012, doi: 10.1002/asia.201200409.

[57] A. Monshi, M. R. Foroughi, and M. R. Monshi, “Modified Scherrer Equation to Estimate More Accurately Nano-Crystallite Size Using XRD,” *World J. Nano Sci. Eng.*, vol. 02, no. 03, pp. 154–160, 2012, doi: 10.4236/wjnse.2012.23020.

[58] S. Habibpour, J. G. Um, Y. seok Jun, P. Bhargava, C. B. Park, and A. Yu, “Structural Impact of Graphene Nanoribbon on Mechanical Properties and Anti-corrosion Performance of Polyurethane Nanocomposites,” *Chem. Eng. J.*, vol. 405, no. September 2020, p. 126858, 2021, doi: 10.1016/j.cej.2020.126858.

[59] M. D. M and R. R. C. D. X-ray, “B O O K REV IE W S,” pp. 543–544, 1990.

[60] R. Saito, M. Hofmann, G. Dresselhaus, A. Jorio, and M. S. Dresselhaus, “Raman spectroscopy of graphene and carbon nanotubes,” *Adv. Phys.*, vol. 60, no. 3, pp. 413–550,

2011, doi: 10.1080/00018732.2011.582251.

[61] L. G. Caņado *et al.*, “General equation for the determination of the crystallite size la of nanographite by Raman spectroscopy,” *Appl. Phys. Lett.*, vol. 88, no. 16, pp. 1–4, 2006, doi: 10.1063/1.2196057.

[62] I. Childres, L. A. Jauregui, W. Park, H. Caoa, and Y. P. Chena, “Raman spectroscopy of graphene and related materials,” *New Dev. Phot. Mater. Res.*, pp. 403–418, 2013.

[63] B. H. Stuart, *Infrared Spectroscopy: Fundamentals and Applications*, vol. 8. 2005.

[64] M. Dittrich, “Chapter 8,” vol. 881, pp. 187–209, 2012, doi: 10.1007/978-1-61779-827-6.

[65] U. M. D. E. C. D. E. Los, *No 主観的健康感を中心とした在宅高齢者における 健康関連指標に関する共分散構造分析Title.* .

[66] W. Han, M. Zheng, A. Banerjee, Y. Z. Luo, L. Shen, and A. Khursheed, “Quantitative material analysis using secondary electron energy spectromicroscopy,” *Sci. Rep.*, vol. 10, no. 1, pp. 1–14, 2020, doi: 10.1038/s41598-020-78973-0.

[67] Y. S. Bae, A. Ö. Yazayd’n, and R. Q. Snurr, “Evaluation of the BET method for determining surface areas of MOFs and zeolites that contain Ultra-Micropores,” *Langmuir*, vol. 26, no. 8, pp. 5475–5483, 2010, doi: 10.1021/la100449z.

[68] F. Ambroz, T. J. Macdonald, V. Martis, and I. P. Parkin, “Evaluation of the BET theory for the characterization of meso and microporous MOFs,” *Small Methods*, vol. 2, no. 11, pp. 1–17, 2018, doi: 10.1002/smtd.201800173.

[69] L. Xu *et al.*, “Pore structure and fractal characteristics of different shale lithofacies in the dalong formation in the western area of the lower yangtze platform,” *Minerals*, vol. 10, no. 1, 2020, doi: 10.3390/min10010072.

[70] Q. Lai, S. Zhu, X. Luo, M. Zou, and S. Huang, “Ultraviolet-visible spectroscopy of

graphene oxides," *Afile///Users/huiyiyang/OneDrive - Univ. Waterloo/Literature Pap. carboxylate graphene .pdfIP Adv.*, vol. 2, no. 3, pp. 2–7, 2012, doi: 10.1063/1.4747817.

[71] P. Majumdar, D. Pant, and S. Patra, "Integrated Photobioelectrochemical Systems: A Paradigm Shift in Artificial Photosynthesis," *Trends Biotechnol.*, vol. 35, no. 4, pp. 285–287, 2017, doi: 10.1016/j.tibtech.2017.01.004.

[72] D. C. Marcano *et al.*, "Improved synthesis of graphene oxide," *ACS Nano*, vol. 4, no. 8, pp. 4806–4814, 2010, doi: 10.1021/nn1006368.

[73] Y. S. Jun *et al.*, "The conductivity of polydimethylsiloxane/graphene nano-ribbon foam composite with elongation," *Carbon N. Y.*, vol. 162, pp. 328–338, 2020, doi: 10.1016/j.carbon.2020.02.024.

[74] S. M. Chang, J. H. Jou, A. Hsieh, T. H. Chen, J. N. Jao, and H. S. Wu, "Internal stress and connection resistance correlation study of microbump bonding," *IEEE Trans. Components Packag. Technol.*, vol. 24, no. 3, pp. 493–499, 2001, doi: 10.1109/6144.946498.

[75] Y. Wang *et al.*, "The Journal of Physical Chemistry C Volume 113 issue 30 2009 [doi 10.1021%2Fjp902214f] Wang, Yan; Shi, Zhiqiang; Huang, Yi; Ma, Yanfeng; Wang, Chengyan -- Supercapacitor Devices Based on Graphene Materials.pdf," *J. Phys. Chem. C*, vol. 113, no. 30 2009, pp. 13103–13107, 2009.

[76] S. Zhang and N. Pan, "Supercapacitors performance evaluation," *Adv. Energy Mater.*, vol. 5, no. 6, pp. 1–19, 2015, doi: 10.1002/aenm.201401401.

[77] Y. Xue *et al.*, "Synthesis of large-area, few-layer graphene on iron foil by chemical vapor deposition," *Nano Res.*, vol. 4, no. 12, pp. 1208–1214, 2011, doi: 10.1007/s12274-011-0171-4.

[78] K. Krishnamoorthy, M. Veerapandian, K. Yun, and S. J. Kim, "The chemical and

structural analysis of graphene oxide with different degrees of oxidation," *Carbon N. Y.*, vol. 53, pp. 38–49, 2013, doi: 10.1016/j.carbon.2012.10.013.

[79] A. C. Ferrari *et al.*, "Raman spectrum of graphene and graphene layers," *Phys. Rev. Lett.*, vol. 97, no. 18, pp. 1–4, 2006, doi: 10.1103/PhysRevLett.97.187401.

[80] S. Some *et al.*, "Can commonly used hydrazine produce n-type graphene?," *Chem. - A Eur. J.*, vol. 18, no. 25, pp. 7665–7670, 2012, doi: 10.1002/chem.201200104.

[81] S. Pisana *et al.*, "Breakdown of the adiabatic Born-Oppenheimer approximation in graphene," *Nat. Mater.*, vol. 6, no. 3, pp. 198–201, 2007, doi: 10.1038/nmat1846.

[82] A. Das *et al.*, "Monitoring dopants by Raman scattering in an electrochemically top-gated graphene transistor," *Nat. Nanotechnol.*, vol. 3, no. 4, pp. 210–215, 2008, doi: 10.1038/nnano.2008.67.

[83] S. Some *et al.*, "High-quality reduced graphene oxide by a dual-function chemical reduction and healing process," *Sci. Rep.*, vol. 3, no. Figure 1, pp. 1–5, 2013, doi: 10.1038/srep01929.

[84] Y. Hwangbo *et al.*, "Interlayer non-coupled optical properties for determining the number of layers in arbitrarily stacked multilayer graphenes," *Carbon N. Y.*, vol. 77, pp. 454–461, 2014, doi: 10.1016/j.carbon.2014.05.050.

[85] V. Kumar, A. Kumar, D. J. Lee, and S. S. Park, "Estimation of number of graphene layers using different methods: A focused review," *Materials (Basel).*, vol. 14, no. 16, 2021, doi: 10.3390/ma14164590.

[86] M. Taha, M. Hassan, S. Essa, and Y. Tartor, "Use of Fourier transform infrared spectroscopy (FTIR) spectroscopy for rapid and accurate identification of Yeasts isolated from human and animals," *Int. J. Vet. Sci. Med.*, vol. 1, no. 1, pp. 15–20, 2013, doi:

10.1016/j.ijvsm.2013.03.001.

[87] V. K. Singh *et al.*, “Fabrication of sensitive bioelectrode based on atomically thin CVD grown graphene for cancer biomarker detection,” *Biosens. Bioelectron.*, vol. 105, pp. 173–181, 2018, doi: 10.1016/j.bios.2018.01.014.

[88] N. M. S. Hidayah *et al.*, “Comparison on graphite, graphene oxide and reduced graphene oxide: Synthesis and characterization,” *AIP Conf. Proc.*, vol. 1892, 2017, doi: 10.1063/1.5005764.

[89] E. Y. Choi *et al.*, “Noncovalent functionalization of graphene with end-functional polymers,” *J. Mater. Chem.*, vol. 20, no. 10, pp. 1907–1912, 2010, doi: 10.1039/b919074k.

[90] S. M. Shinde, E. Kano, G. Kalita, M. Takeguchi, A. Hashimoto, and M. Tanemura, “Grain structures of nitrogen-doped graphene synthesized by solid source-based chemical vapor deposition,” *Carbon N. Y.*, vol. 96, pp. 448–453, 2016, doi: 10.1016/j.carbon.2015.09.086.

[91] W. Wu *et al.*, “Growth of single crystal graphene arrays by locally controlling nucleation on polycrystalline Cu using chemical vapor deposition,” *Adv. Mater.*, vol. 23, no. 42, pp. 4898–4903, 2011, doi: 10.1002/adma.201102456.

[92] L. W. Le Fevre, J. Cao, I. A. Kinloch, A. J. Forsyth, and R. A. W. Dryfe, “Systematic Comparison of Graphene Materials for Supercapacitor Electrodes,” *ChemistryOpen*, vol. 8, no. 4, pp. 418–428, 2019, doi: 10.1002/open.201900004.

[93] F. R. Sultanov *et al.*, “Microwave-enhanced chemical vapor deposition graphene nanoplatelets-derived 3D porous materials for oil/water separation,” *Carbon Lett.*, vol. 30, no. 1, pp. 81–92, 2020, doi: 10.1007/s42823-019-00073-5.

[94] S. Lim, H. Park, G. Yamamoto, C. Lee, and J. W. Suk, “Measurements of the electrical

conductivity of monolayer graphene flakes using conductive atomic force microscopy," *Nanomaterials*, vol. 11, no. 10, 2021, doi: 10.3390/nano11102575.

[95] Ö. B. Mergen, E. Umut, E. Arda, and S. Kara, "A comparative study on the AC/DC conductivity, dielectric and optical properties of polystyrene/graphene nanoplatelets (PS/GNP) and multi-walled carbon nanotube (PS/MWCNT) nanocomposites," *Polym. Test.*, vol. 90, p. 106682, 2020, doi: 10.1016/j.polymertesting.2020.106682.

[96] M. J. Deka, U. Baruah, and D. Chowdhury, "Insight into electrical conductivity of graphene and functionalized graphene: Role of lateral dimension of graphene sheet," *Mater. Chem. Phys.*, vol. 163, pp. 236–244, 2015, doi: 10.1016/j.matchemphys.2015.07.036.

[97] R. G. Oxide, E. Analysis, and Q. Control, "Reduced Graphene Oxide : Properties , Applications and Production Methods Graphene Oxide to Reduced Graphene Oxide," pp. 1–5, 2015.

[98] S. M. S. Al-Mufti, A. Almontasser, and S. J. A. Rizvi, "Single and double thermal reduction processes for synthesis reduced graphene oxide assisted by a muffle furnace: A facile robust synthesis and rapid approach to enhance electrical conductivity," *AIP Adv.*, vol. 12, no. 12, 2022, doi: 10.1063/5.0128803.

[99] Y. U. Shang, D. Zhang, Y. Liu, and C. Guo, "Preliminary comparison of different reduction methods of graphene oxide," *Bull. Mater. Sci.*, vol. 38, no. 1, pp. 7–12, 2015, doi: 10.1007/s12034-014-0794-7.

[100] Q. Wu *et al.*, "Cyclic stability of supercapacitors: materials, energy storage mechanism, test methods, and device," *J. Mater. Chem. A*, vol. 9, no. 43, pp. 24094–24147, 2021, doi: 10.1039/d1ta06815f.